

SGK1 drives hippocampal demyelination and diabetes-associated cognitive dysfunction in mice

Received: 3 December 2023

Accepted: 31 January 2025

Published online: 17 February 2025

 Check for updates

Ziying Jiang^{1,12}, Bin Liu^{2,12}, Tangsheng Lu^{3,12}, Xiaoxing Liu⁴, Renjun Lv^{5,6}, Kai Yuan⁴, Mengna Zhu⁷, Xinning Wang⁷, Shangbin Li⁵, Song Xu⁵, Xinyu Wang⁵, Yifei Wang⁵, Zhenfang Gao⁷, Peiqing Zhao⁸, Zongyong Zhang⁷, Junwei Hao^{1,9,10}✉, Lin Lu^{3,4,11}✉ & Qingqing Yin⁶✉

Diabetes-associated cognitive dysfunction (DACD) is increasingly recognized as a critical complication of diabetes. The complex pathology of DACD remains unknown. Here, we performed single-nucleus RNA sequencing (snRNA-seq) to demonstrate unique cellular and molecular patterns of the hippocampus from a mouse model of diabetes. More in-depth analysis of oligodendrocytes (OLs) distinguished five subclusters, indicating different functional states of OLs and transcriptional changes in each subcluster. Based on the results of snRNA-seq and experiments in vivo, we observed demyelination and disharmony of oligodendroglial lineage cell composition in male diabetic mice. Serum/glucocorticoid regulated kinase 1 (SGK1) expression was significantly increased in the hippocampus OLs of male diabetic mice, and SGK1 knockdown in hippocampus reversed demyelination and DACD via N-myc downstream-regulated gene 1 (NDRG1)-mediated pathway. The findings illustrated a transcriptional landscape of hippocampal OLs and substantiated impaired myelination in DACD. Our results provided direct evidence that inhibition of SGK1 or the promotion of myelination might be a potential therapeutic strategy for DACD.

Diabetes mellitus (DM) has become a global public health problem on account of the rising prevalence and complex complications¹. Diabetes-associated cognitive dysfunction (DACD) was common but easily overlooked among the variety of complications of DM^{2,3}.

Epidemiological studies have established that participants with DM had a higher risk (about 20% to 60%) for developing all-cause cognitive impairments compared to nondiabetic individuals^{2,4}. The cognitive dysfunction of DM individuals, especially type 2 diabetes mellitus

¹Department of Neurology, Xuanwu Hospital, National Center for Neurological Disorders, Capital Medical University, Beijing, China. ²Department of Neurology, The First Affiliated Hospital of Shandong First Medical University & Shandong Provincial Qianfoshan Hospital, Shandong Institute of Neuroimmunology, Jinan, Shandong, China. ³National Institute on Drug Dependence and Beijing Key Laboratory of Drug Dependence Research, Peking University, Beijing, China. ⁴Peking University Sixth Hospital, Peking University Institute of Mental Health, NHC Key Laboratory of Mental Health (Peking University), National Clinical Research Center for Mental Disorders (Peking University Sixth Hospital), Beijing, China. ⁵Department of Geriatrics, Shandong Provincial Hospital Affiliated to Shandong First Medical University, Jinan, Shandong, China. ⁶Department of Geriatric Neurology, Shandong Provincial Hospital Affiliated to Shandong First Medical University, Jinan, Shandong, China. ⁷Institute of Brain Science and Brain-inspired Research, Shandong First Medical University & Shandong Academy of Medical Sciences, Jinan, Shandong, China. ⁸Department of Translational Medical Center, Zibo Central Hospital Affiliated to Binzhou Medical University, Zibo, Shandong, China. ⁹Beijing Municipal Geriatric Medical Research Center, Beijing, China. ¹⁰Key Laboratory for Neurodegenerative Diseases of Ministry of Education, Beijing, China. ¹¹Peking-Tsinghua Center for Life Sciences and PKU-IDG/McGovern Institute for Brain Research, Peking University, Beijing, China. ¹²These authors contributed equally: Ziying Jiang, Bin Liu, Tangsheng Lu. ✉e-mail: haojunwei@vip.163.com; linlu@bjmu.edu.cn; yinqingqing@sdfmu.edu.cn

(T2DM), is mainly manifested in memory, executive function, processing speed, attention and other cognitive domains. The etiology of DACD is multi-factorial, such as brain insulin resistance, disordered glucolipid metabolism, brain microvascular injury, mitochondrial dysfunction, and neuroinflammation^{5,6}. However, a randomized clinical trial has disclosed that a standard therapeutic strategy to control blood glucose has limited beneficial effects on cognitive decline induced by T2DM⁷. Therefore, clarifying the pathological mechanism and exploring effective prevention and treatment strategies for DACD was urgent and necessitated further action^{8,9}.

Loss of myelinated nerve fibers induced by hyperglycemia, insulin deficiency and obesity has been considered the driving force underlying the occurrence and development of diabetic neuropathy, especially in the peripheral nerves^{10,11}. Emerging evidence during the last decade suggested that demyelination also participated in the central nervous system (CNS) of clinical and experimental diabetic research^{12,13}. In addition, it has been widely acknowledged that myelin sheaths and oligodendroglial lineage cells have a critical impact on regulating cognitive dysfunction and neurodegenerative diseases, such as Alzheimer's disease (AD)¹⁴. Nonetheless, direct evidence presenting the involvement of demyelination and oligodendrocyte (OL) status in DACD has been uncovered, and the potential mechanism remains unknown.

Analysis of molecular signatures responses in the hippocampus, a region key for learning, memory, and cognition ability, is an appropriate access to elucidate the pathological process of DACD¹⁵. Single-nucleus RNA sequencing (snRNA-seq) is a novel practical approach that allows transcriptomic profiling of each single nucleus, identifies cell subclusters and defines their distinguishing characteristics¹⁶. In the present study, we performed snRNA-seq to comprehensively characterize the composition and transcriptional changes in the hippocampus tissue of the diabetic mice model. Based on integrated data, we identified diverse cell types in the hippocampus and filtrated differentially expressed genes (DEGs) in diverse cell types. After revealing the genic heterogeneity and diversity of OLs, we confirmed that demyelination could be a critical pathophysiological driver of DACD progression, including oligodendrocyte precursor cell (OPC) differentiation and OL apoptosis. Intriguingly, the myelin deficits of DACD were associated with serum/glucocorticoid regulated kinase 1 (SGK1) and N-myc downstream-regulated gene 1 (NDRG1) signal pathway in OLs.

Results

snRNA-seq analysis reveals the cell composition of the hippocampus in *db/db* mice

Firstly, we evaluated the blood glucose and cognitive performance of two diabetic models, *db/db* mice and high-fat diet (HFD)-fed mice, to study DACD. Body weight and fasting blood glucose of control (*db/m*) and diabetic (*db/db*) groups were recorded at 20 weeks of age (Supplementary Fig. 1a, b). Then we performed the nest building test, novel object recognition (NOR) test, and morris water-maze (MWM) test to evaluate spontaneous behaviors, learning and memory performance. We found that *db/db* mice presented significant cognitive impairment, including lower nest score, lower discrimination index, longer escape latency, shorter time in the target quadrant, and lesser passing time for crossing the platform location (Supplementary Fig. 1c–i). Consistent with previous studies^{17,18}, the swimming speed of *db/db* mice was slower than that of *db/m* mice, possibly affecting the outcomes of the MWM test. We further demonstrated the motor activity (walking speed) of *db/db* mice was not damaged compared to the *db/m* mice (Supplementary Figs. 1j, k). Similar results were also detected in the HFD-fed mice (Supplementary Fig. 2).

We collected fresh hippocampus from *db/m* and *db/db* mice for snRNA-seq analysis (Fig. 1a), and a total of 23,016 single nuclei were sequenced. After filtering low-quality nuclei, 20,690 high-quality

nuclei were obtained for subsequent biological analysis (12,104 from the control group and 8586 from the diabetic group, respectively). Reducing single nuclei populations in *db/db* mice might be associated with brain atrophy induced by diabetes. Consistently with other research^{19–21}, we observed the distinct hippocampus atrophy in *db/db* mice by evaluating the hippocampus thickness and weights (Supplementary Figs. 1l, m).

To validate the nucleus sequencing data, we checked the *Malat1* expression, a common nuclear-located RNA, and found high *Malat1* levels of each cluster in the major seven cell types of our nucleus sequencing data (Supplementary Fig. 3a). Based on the acknowledged cell type-specific markers, 27 clusters were classified into 7 major cell types, neurons (*Gad1*, *Gad2*, *Atp1b1*, and *Rtn1*), OLs (*Mal*, *Mbp*, *Mobp*, and *Mog*), OPCs (*Pdgfra*), endothelial cells (*Bsg* and *Flt1*), microglia (*C1qa*, *C1qb*, and *C1qc*), fibroblasts (*Col3a1*, *Dcn*, and *Fstl1*), and astrocytes (*Aqp4*, *Slc1a2*, and *Slc1a3*) (Figs. 1b, c and Supplementary Fig. 3b–h). snRNA-seq results uncovered the dramatic shifts of cellular composition in the two groups. Compared to the control group, the relative abundance of OLs was remarkably decreased, while microglia and astrocytes were increased in the diabetic group (Fig. 1d, e). To verify the fidelity of the snRNA-seq results, we subsequently conducted flow cytometry of hippocampus from two diabetic mouse models (Supplementary Fig. 4a). We found that the results of the two methods were consistent in the numbers and variations of multiple cell types, including neurons, OLs, OPCs, microglia, and astrocytes (Figs. 1f–j and Supplementary Fig. 4b, c).

Diabetes altered gene expression in diverse cell types of the hippocampus in *db/db* mice. Based on the snRNA-seq data, we analyzed the specific genes in diverse cell types in order to investigate the pathomechanism of DACD. Overall, 5,817 genes were up-regulated, and 2699 genes were down-regulated in two groups (Supplementary Fig. 5a). Top 50 differentially expressed genes (DEGs, 25 up- and 25 down-regulated) of diverse cell types between control and diabetic hippocampal cells were ascertained and shown using heat maps (Supplementary Figs. 5b–h). Kyoto Encyclopedia of Genes and Genomes (KEGG) pathway enrichment analysis predicted pathways of diverse cell types involved in diabetes based on identified DEGs. All kinds of cells of hippocampus are primarily associated with oxidative phosphorylation, Parkinson's disease (PD), Huntington's disease (HD), AD, thermogenesis, retrograde endocannabinoid signaling, and ribosome (Supplementary Fig. 6a). We detailed demonstrated the TOP 10 enrichment pathways in different cell types (Supplementary Fig. 6b–h).

We also conducted the cell-cell communication analysis to diagram cellular interaction networks. Neurons, OLs and OPCs were the most active cell types in *db/m* and *db/db* mice (Supplementary Fig. 7a). Moreover, the numbers of ligand-receptor pairs in *db/db* mice were increased entirely compared with those in *db/m* mice. The top ligand-receptor pairs in two groups were exhibited, such as *Nrxn3-Nlgn1*, *Nrxn1-Nlgn1*, *Ncam1-Ncam2*, and *Cntn1-Nrcam* (Supplementary Figs. 7b, c).

Interestingly, we noticed a dramatic change in OLs, known as the central myelinating cells of the CNS, indicating myelination might be closely related to the development of DACD. Therefore, we further analyzed the expression levels of myelin-related genes in different cell types. *Mbp* (a common marker of myelin) and *Sox10* (effective regulator of myelination) RNA expression levels were significantly decreased in OLs of *db/db* mice, compared with *db/m* mice. Transcriptional levels of other myelin-related genes, including *Myrf* and *Dlg4*, were exhibited in Supplementary Fig. 8.

Subcluster analysis indicates the difference of OLs of the hippocampus in *db/db* mice

Considering the possible important role of demyelination on DACD progression, we further performed a particular subcluster analysis of

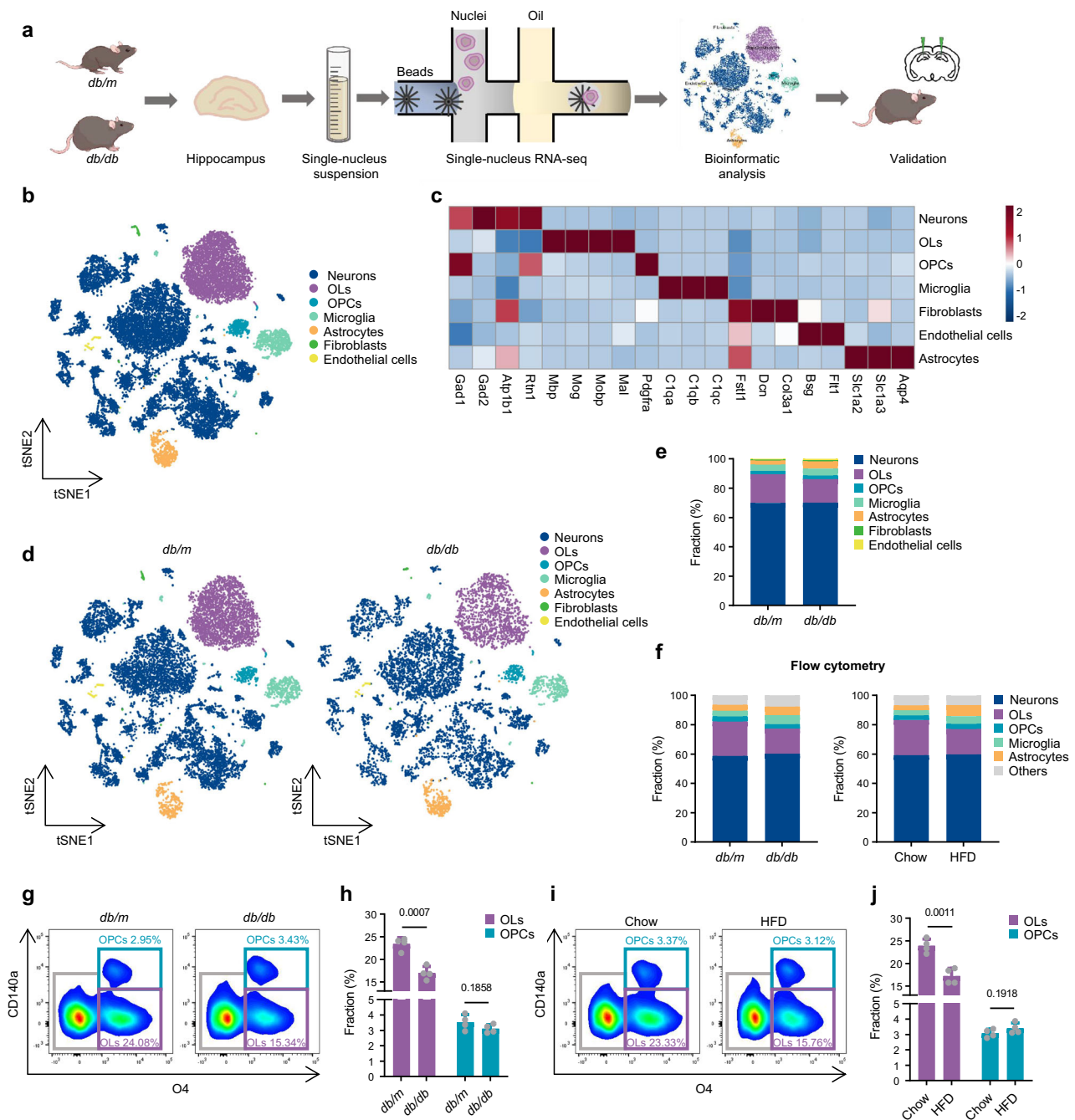


Fig. 1 | snRNA-seq analysis revealed the cell composition of the hippocampus in *db/db* mice. a Schematic depicting our study design. **b** t-SNE plot presenting the different cell types of the hippocampus. **c** Heat map showing well-established gene marker expression to identify cell clusters. **d** t-SNE plot and **e** bar chart presenting the relative abundances of different cell types from the *db/m* and *db/db* mice. **f** Bar chart presenting the relative abundances of different cell types from the diabetic and control mice by flow cytometry, $n = 4$ mice per group. **g** Representative FACS

plots of OLs and OPCs in hippocampus from *db/m* and *db/db* mice. **h** Quantification of FACS analysis from (**g**), $n = 4$ mice per group. **i** Representative FACS plots of OLs and OPCs in hippocampus from HFD or Chow-fed mice. **j** Quantification of FACS analysis from (**i**), $n = 4$ mice per group. Data are presented as mean \pm SEM, and analyzed by unpaired two-tailed Student's t -tests. Source data are provided as a Source data file. HFD, high-fat diet; OLs, oligodendrocytes; OPCs, oligodendrocyte precursor cells.

OLs to reveal heterogeneity within OLs. According to the published database^{22,23}, the above-mentioned OPCs and OLs were identified into 5 subclusters to depict the differentiation and mature process of OLs. The 5 subclusters included (1) OPCs (*Cspg4* and *Pdgfra*), (2) differentiation-committed oligodendrocyte precursors (COP) and newly formed oligodendrocytes (NFOL) (*Bmp4*, *Casr*, and *Tcf7l2*), (3) myelin-forming oligodendrocytes (MFOL) (*Ablims* and *Tmem141*), (4) mature oligodendrocytes 1 (MOL1) (*Ptgds*, *Opalin*, and *Il33*), (5) MOL2 (*Klk6*, *Apod*, and *Cd59a*). We showed the heat map of marker

expression in diverse OL subclusters and performed the significance test in MOL1 and MOL2. There was a highly significant difference in cell markers among the MOL1 and MOL2 groups (all $p < 0.01$; Fig. 2a, b; Supplementary Fig. 9a, b). Fluorescence in situ hybridization (FISH) was performed to assess the colocalization of the OL marker (*Mbp*) and MOL markers (*Ptgds* and *Klk6*). The results showed that MOL1 populations (*Ptgds*⁺) were distinct from MOL2 (*Klk6*⁺) (Supplementary Fig. 9c). Obviously, the populations of different oligodendroglial lineage cell subclusters in *db/db* mice were decreased sharply

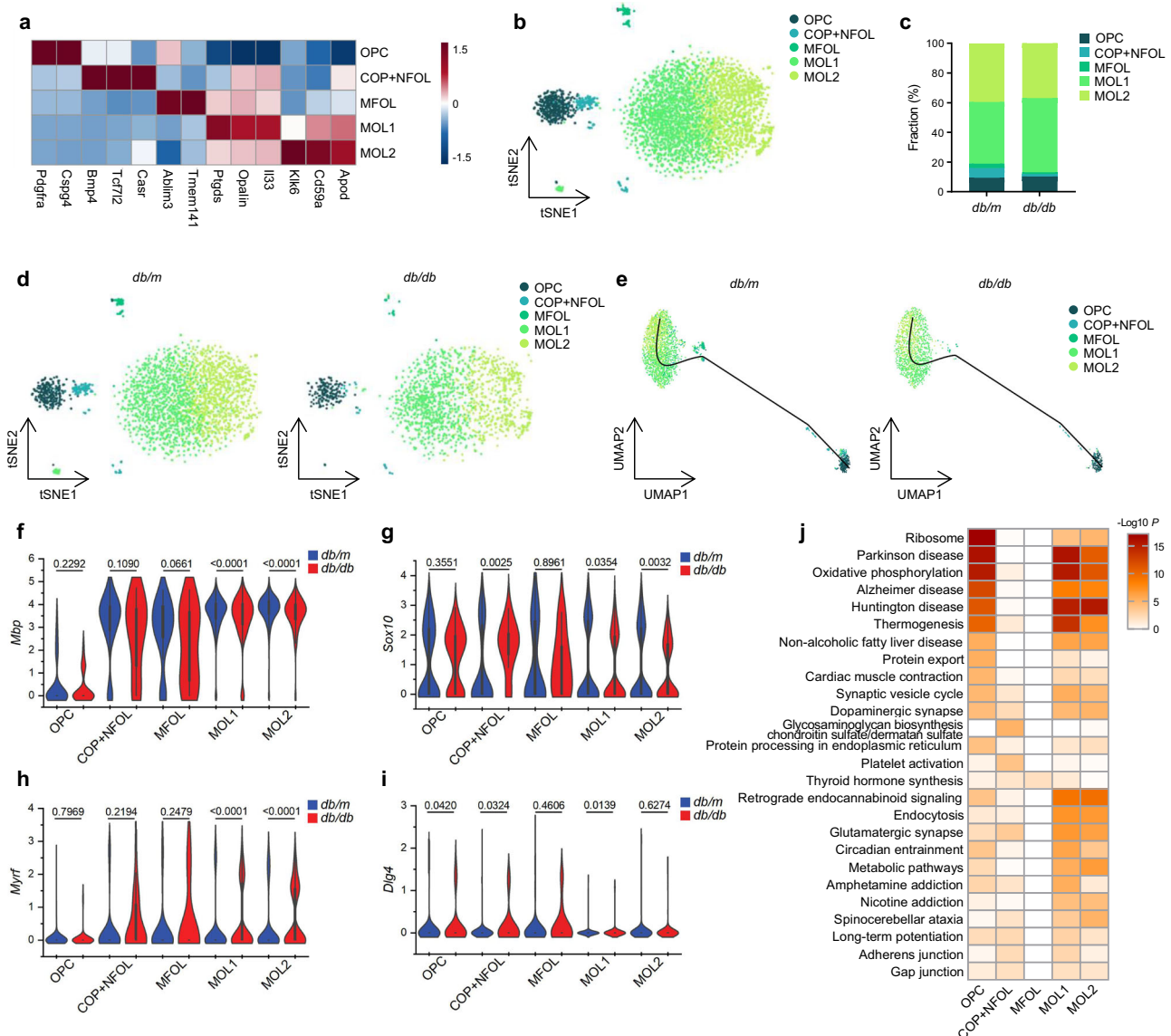


Fig. 2 | Subcluster analysis indicated the difference in OLs of the hippocampus in *db/db* mice. **a** Heat map showing well-established gene marker expression to identify oligodendrocyte subclusters. **b** t-SNE plot presenting the oligodendrocyte subclusters of the hippocampus. **c** Bar chart and **d** t-SNE plot presenting relative abundances of oligodendrocyte subclusters from the *db/m* and *db/db* mice. **e** Differentiation trajectories of these subclusters were analyzed using Slingshot. Violin plot showing the expression of myelin-related genes (**f**) *Mbp*, (**g**) *Sox10*, (**h**) *Myrf* and (**i**) *Dlg4* in the oligodendrocyte subclusters. **j** Heat map showing

presenting the representative KEGG enrichment pathways in oligodendrocyte subclusters. Data are analyzed by unpaired two-tailed Student's *t*-tests for (**f**–**i**) and hypergeometric test for (**j**). Source data are provided as a Source data file. COP, differentiation-committed oligodendrocyte precursors; KEGG, Kyoto Encyclopedia of Genes and Genomes; MFOL, myelin-forming oligodendrocytes; MOL, mature oligodendrocytes; NFOL, newly formed oligodendrocytes; OPC, oligodendrocyte precursor cell.

compared to the *db/m* mice. Compared to the *db/m* mice, the relative abundance of COP + NFOL, MFOL and MOL2 was significantly decreased in the *db/db* mice. On the other hand, the relative abundance of OPC and MOL1 was significantly increased in the *db/db* mice (Figs. 2c, d and Supplementary Fig. 9d). Pseudo-temporal analysis was performed to identify the dynamics of OL lineage cells in DACD progression, showing the lineage transitions of OPC, COP and NFOL to MOLs in *db/db* mice hippocampus (Fig. 2e).

The integrated data of subcluster analysis presented unique transcriptional profiles and cellular heterogeneity of oligodendroglial lineage cells as expected (Supplementary Fig. 10). Top 30 DEGs (15 up- and 15 down-regulated) of different oligodendroglial lineage cell subclusters between *db/m* and *db/db* hippocampus were determined and demonstrated using heat maps. Similar with the myelin-related genes alterations in OLs, *Mbp* gene was down-regulated in MOL1 and MOL2 of

db/db mice, compared to *db/m* mice (Fig. 2f). *Sox10* expression levels were reduced in COP + MFOL, MOL1 and MOL2, *Myrf* expression levels were reduced in MOL1 and MOL2, *Dlg4* expression levels were reduced in OPC, COP + MFOL and MOL1 of *db/db* mice, compared to *db/m* mice (Fig. 2g–i). KEGG analysis of oligodendroglial lineage cell subclusters revealed abundant pathways involved in diabetes, such as ribosome, PD, oxidative phosphorylation, HD, thermogenesis, and AD (Fig. 2j). We also exhibited the TOP 10 enrichment pathways in each subcluster (Supplementary Fig. 11).

Demyelination is involved in DACD of diabetic mice

The snRNA-seq results demonstrated that demyelination was involved in DACD, therefore, we detected myelination-related indicators in diabetic mice. Firstly, Luxol fast blue (LFB) staining was performed to verify reduced myelination in the corpus callosum, hippocampus

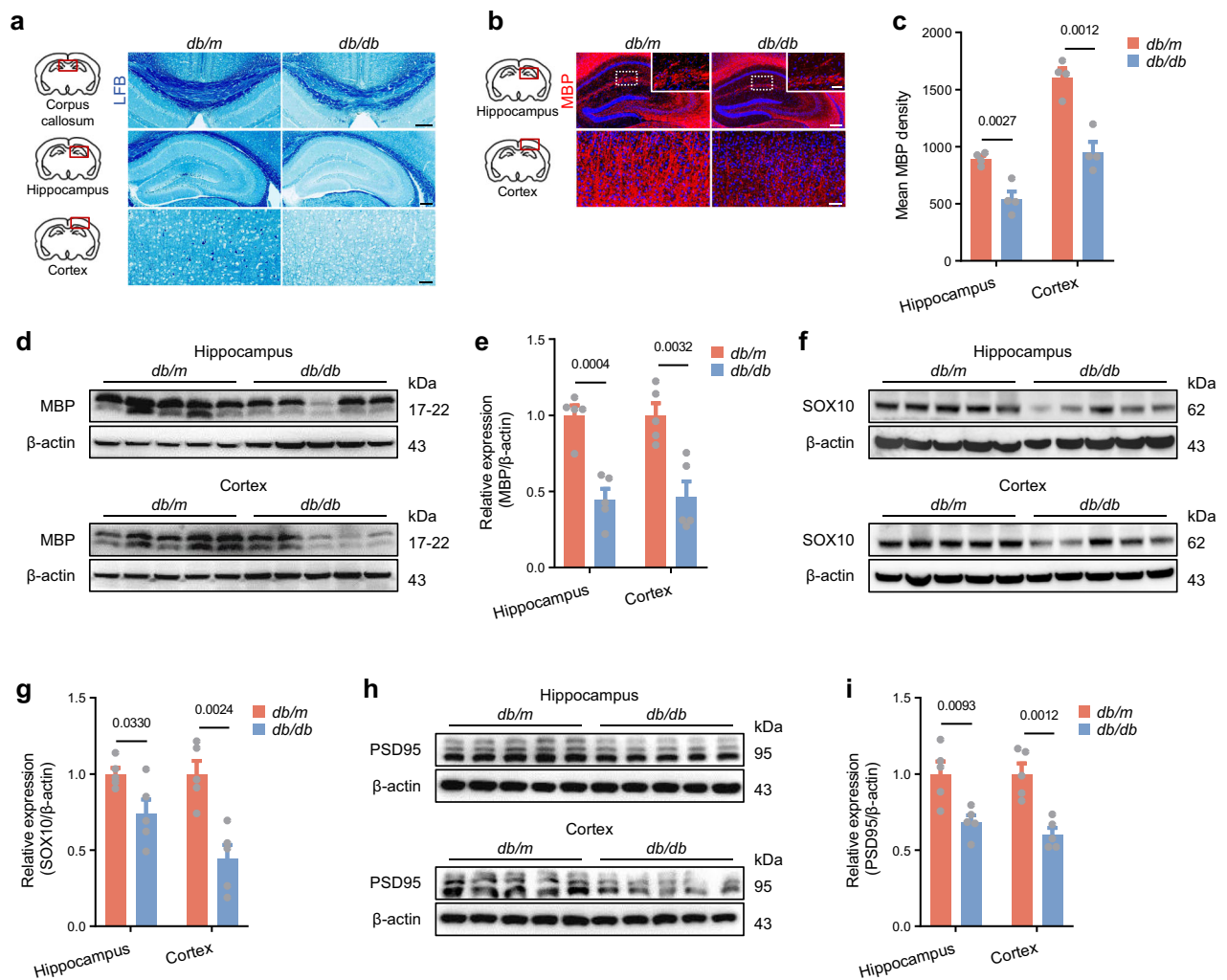


Fig. 3 | Myelination was reduced in the hippocampus of *db/db* mice.

a Representative images of LFB staining in *db/m* and *db/db* mice. Scale bar: 200 μ m (corpus callosum, hippocampus) and 50 μ m (cortex). **b** Representative immunofluorescence images of MBP expression in *db/m* and *db/db* mice. Scale bar: 200 μ m and 50 μ m (hippocampus), and 50 μ m (cortex). **c** Quantification of immunofluorescence images from (b), $n = 4$ mice per group. **d** Western blot analysis of the expression of MBP in *db/m* and *db/db* mice. **e** Quantification of protein bands from

(d), $n = 5$ mice per group. **f** Western blot analysis of the expression of SOX10 in *db/m* and *db/db* mice. **g** Quantification of protein bands from (f), $n = 5$ mice per group. **h** Western blot analysis of the expression of PSD95 in *db/m* and *db/db* mice. **i** Quantification of protein bands from (h), $n = 5$ mice per group. Data are presented as mean \pm SEM, and analyzed by unpaired two-tailed Student's *t*-tests. Source data are provided as a Source data file. LFB, Luxol fast blue.

and cortex of *db/db* mice (Fig. 3a). In addition, we used immunofluorescence analysis and western blot analysis to evaluate the MBP in the brain of *db/db* mice. The results showed that MBP levels were significantly decreased both in the hippocampus and cortex of the *db/db* group compared to the *db/m* group (Fig. 3b–e). Finally, we measured the SOX10 (effective myelination regulator) and PSD95 (vital synaptic protein) levels using western blot analysis. Analogously, both SOX10 and PSD95 expressions were reduced in the hippocampus and cortex of the diabetic group compared to the control group (Fig. 3f–i).

Analogous demyelinating features were captured in the HFD-fed mice (Fig. 4a–i). Transmission electron microscopy (TEM) visualized the ultra-structural myelination status of HFD-fed mice; the myelin sheath in the diabetic group was thin, loose and irregularly shaped compared to those in the control group (Fig. 4j, k). The g-ratio (ratio of the inner to the outer boundary of a myelinated axon) in HFD-fed mice were higher than in Chow-fed mice, suggesting diabetes contributed to thinner myelin sheath (Fig. 4l). Moreover, we implemented TEM to observe the synapse status in the hippocampus at the ultra-structural level. The HFD-fed mice were found synaptic deficits, such as fewer

asymmetric synapses per field and thinner postsynaptic density, compared to the control mice (Fig. 4m–o). These results confirmed that demyelination might participate in the pathological process of DACD.

To further investigate the alteration of oligodendroglial lineage cells in diabetic brains, we measured the population marker by OLIG2, OPCs marked by PDGF receptor α (PDGFR α), and mature OLs marked by CC1. The number of PDGFR α ⁺OLIG2⁺ OPC remained unchanged in the corpus callosum, hippocampus and cortex between the *db/db* mice and *db/m* mice (Supplementary Fig. 12). The number of CC1⁺OLIG2⁺ OLs was reduced in the corpus callosum, hippocampus and cortex of *db/db* mice (Fig. 5a, b). To probe the differentiation and/or apoptosis in OLs, we administered 5-ethynyl-2'-deoxyuridine (EdU) to trace the new OLs and performed a TUNEL assay of OLs, respectively. The density of EdU⁺CC1⁺ cells significantly decreased in the corpus callosum, hippocampus and cortex of *db/db* mice (Fig. 5c, d). Furthermore, the proportion of apoptotic OLs was evidently increased in *db/db* mice (Fig. 5e, f). Consistent findings were observed in HFD-fed mice (Supplementary Fig. 13a–h). All the results collectively indicated the disturbances of OPC differentiation and OL survival in diabetic brains.

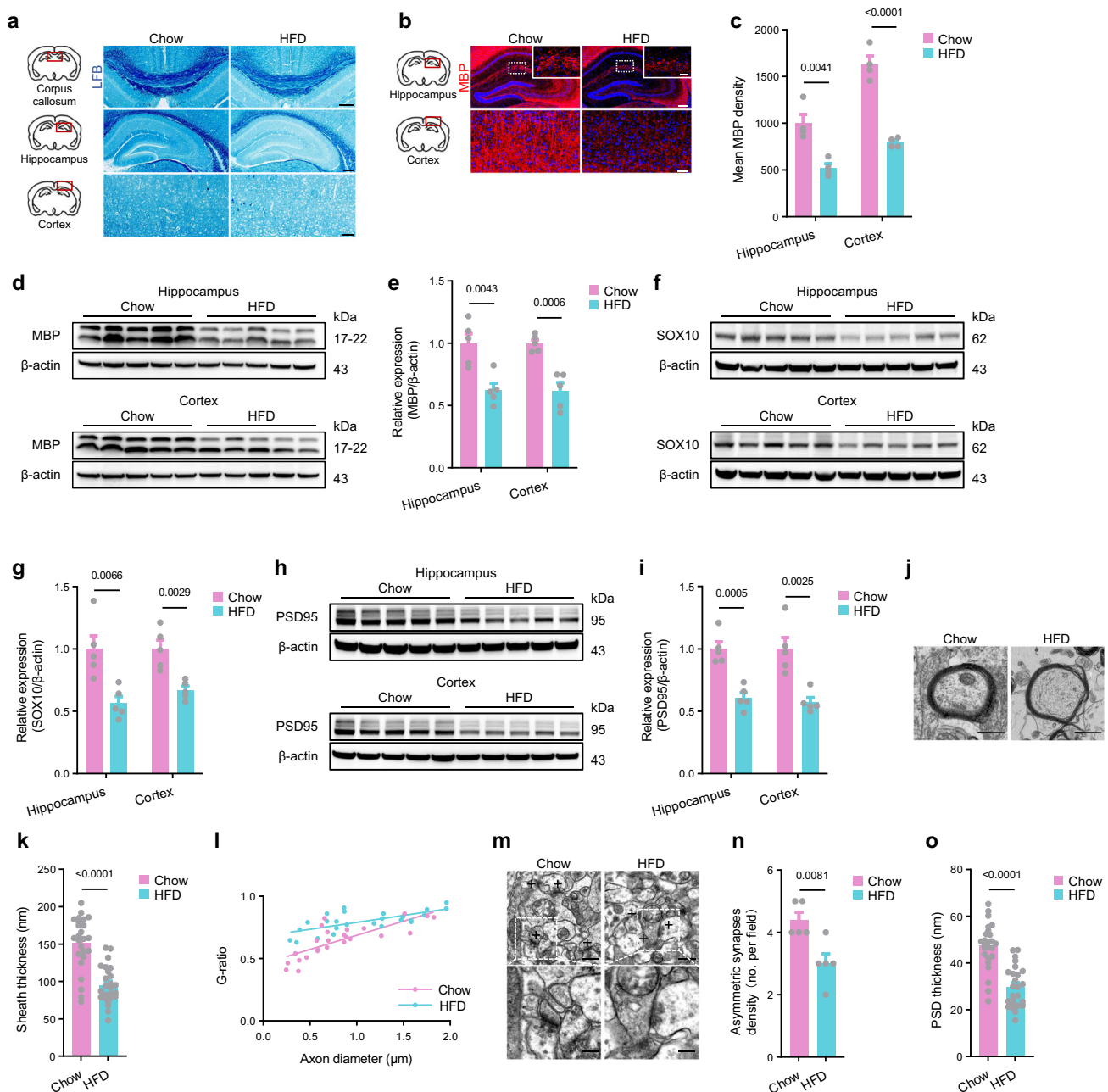


Fig. 4 | Myelination was reduced in the hippocampus of HFD-fed mice.

a Representative images of LFB staining in Chow or HFD-fed mice. Scale bar: 200μm (corpus callosum, hippocampus) and 50μm (cortex). **b** Representative immunofluorescence images of MBP expression in Chow or HFD-fed mice. Scale bar: 200μm and 50μm (hippocampus), and 50μm (cortex). **c** Quantification of immunofluorescence images from (b), ($n = 4$ mice per group). **d** Western blot analysis of the expression of MBP in Chow or HFD-fed mice. **e** Quantification of protein bands from (d), $n = 5$ mice per group. **f** Western blot analysis of the expression of SOX10 in Chow or HFD-fed mice. **g** Quantification of protein bands from (f), $n = 5$ mice per group. **h** Western blot analysis of the expression of PSD95 in Chow or HFD-fed mice. **i** Quantification of protein bands from (h), $n = 5$ mice per

group. **j** Representative electron micrographs of myelinated axons of the hippocampus from different groups. Scale bar: 500 nm. **k** Bar chart showed sheath thickness from different groups. **l** Scatter plot showed g-ratio from different groups, $n = 5$ images from 5 mice per group. **m** Representative electron micrographs of synapses of the hippocampus from different groups. Scale bar: 500 nm and 200 nm. **n** Bar chart showed the numbers of asymmetric synapses from different groups, $n = 5$ mice per group. **o** Bar chart showed PSD thickness from different groups, $n = 5$ images from 5 mice per group. Data are presented as mean \pm SEM, and analyzed by unpaired two-tailed Student's t -tests. Source data are provided as a Source data file. HFD, high-fat diet; LFB, Luxol fast blue.

Recent research has shown that myelin changes dynamically in the adult brain²⁴. OPCs differentiate into newly generated OLs and then form myelin sheaths, which might accompany the degeneration of pre-existing myelin sheaths. Therefore, we labelled and traced newly generated myelin and pre-existing myelin separately to understand the myelin dynamics in diabetic mice. The NG2-CreERT; Tau-mGFP mice

line was employed to label the newly formed myelin sheaths²⁵. Tamoxifen (TMF) can induce Tau-mGFP alleles recombination in NG2⁺ OPCs, and the mGFP expression is controlled by the Tau promoter. Considering Tau is highly expressed in OLs while rarely low in OPCs, membrane-bound GFP (mGFP, green) can only be visualized in newly generated OLs and myelin sheaths. 7-week-old NG2-CreERT; Tau-mGFP

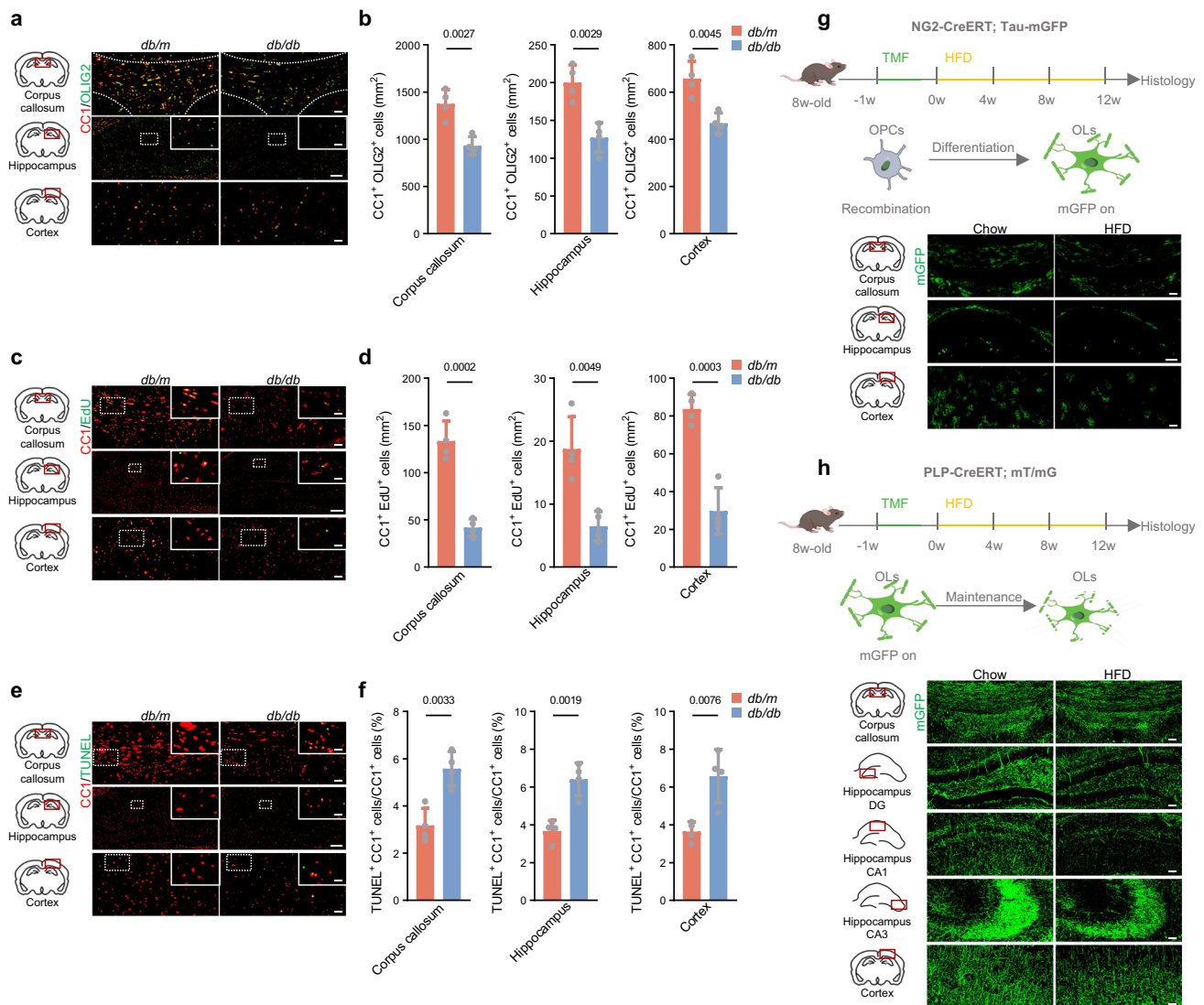


Fig. 5 | Differentiation and apoptosis of OLs were disturbed in the hippocampus of diabetic mice. **a** Representative immunofluorescence images of CC1 and OLIG2-labeling OLs in *db/m* and *db/db* mice. Scale bar: 50μm (corpus callosum), 200μm and 50μm (hippocampus), 50μm (cortex). **b** Quantification of immunofluorescence images from (a), *n* = 4 mice per group. **c** Representative immunofluorescence images of CC1 and EdU-labeling new OLs in *db/m* and *db/db* mice. Scale bar: 50μm and 25μm (corpus callosum), 200μm and 25μm (hippocampus), 50μm and 25μm (cortex). **d** Quantification of immunofluorescence images from (c), *n* = 4 mice per group. **e** Representative immunofluorescence images of CC1 and TUNEL-labeling apoptotic OLs in *db/m* and *db/db* mice. Scale bar: 50μm and 25μm (corpus callosum), 200μm and 25μm (hippocampus), 50μm and 25μm (cortex). **f** Quantification of immunofluorescence images from (e), *n* = 4 mice per group. **g** Representative immunofluorescence images of mGFP-positive myelin in HFD-fed NG2-CreERT; Tau-mGFP mice. Scale bar: 50μm (corpus callosum), 200μm (hippocampus), 50μm (cortex). **h** Representative immunofluorescence images of mGFP-positive myelin in HFD-fed PLP-CreERT; mT/mG mice. Scale bar: 50μm (corpus callosum, hippocampus, cortex). Data are presented as mean ± SEM, and analyzed by unpaired two-tailed Student's *t*-tests. Source data are provided as a Source data file. CA, cornu ammonis; DG, dentate gyrus; EdU, 5-ethynyl-2'-deoxyuridine; HFD, high-fat diet; OLs, oligodendrocytes; OPCs, oligodendrocyte precursor cells; TMF, Tamoxifen.

(cortex). **f** Quantification of immunofluorescence images from (e), *n* = 4 mice per group. **g** Representative immunofluorescence images of mGFP-positive myelin in HFD-fed NG2-CreERT; Tau-mGFP mice. Scale bar: 50μm (corpus callosum), 200μm (hippocampus), 50μm (cortex). **h** Representative immunofluorescence images of mGFP-positive myelin in HFD-fed PLP-CreERT; mT/mG mice. Scale bar: 50μm (corpus callosum, hippocampus, cortex). Data are presented as mean ± SEM, and analyzed by unpaired two-tailed Student's *t*-tests. Source data are provided as a Source data file. CA, cornu ammonis; DG, dentate gyrus; EdU, 5-ethynyl-2'-deoxyuridine; HFD, high-fat diet; OLs, oligodendrocytes; OPCs, oligodendrocyte precursor cells; TMF, Tamoxifen.

mice were administered intragastrically with TMF and then fed with HFD for 12 consecutive weeks to induce DACD. Compared to control mice, the mGFP⁺ myelin sheaths were significantly decreased in the corpus callosum, cortex, and hippocampus of HFD-fed mice (Fig. 5g and Supplementary Fig. 13i). In addition, we obtained PLP-CreERT; mT/mG mice line to label and trace the pre-existing myelin sheaths²⁶. As a vital myelin-related protein, PLP is only expressed in mature OLs but not newly-formed OLs. After recombination induced by TMF, mGFP can express in pre-existing OLs and myelin sheaths. Consistently, the area of mGFP⁺ myelin was reduced in the corpus callosum, cortex, and hippocampus of HFD-fed mice (Fig. 5h and Supplementary Fig. 13j). Together, these results demonstrated that new myelin generation was inhibited in combination with accelerating degradation of pre-existing

myelin in diabetic brains, ultimately leading to myelin dysfunction and dyshomeostasis in DACD mouse models.

Increased SGK1 expression is associated with demyelination in diabetic mice

We concentrated on the DEGs data of snRNA-seq analysis to identify particular genes that modulate demyelination in diabetic mice. As the top DEG in OLs, *Sgk1* was found to be present predominantly in OLs of *db/db* mice and significantly up-regulated in OLs, OPCs, and microglia of *db/db* mice (Fig. 6a, b). We next analyzed the distribution of *Sgk1* across different OLs subclusters in which finding *Sgk1* was over-expressed in all kinds of OLs subclusters of *db/db* mice (Fig. 6c, d), suggesting the crucial role in the development of OLs and

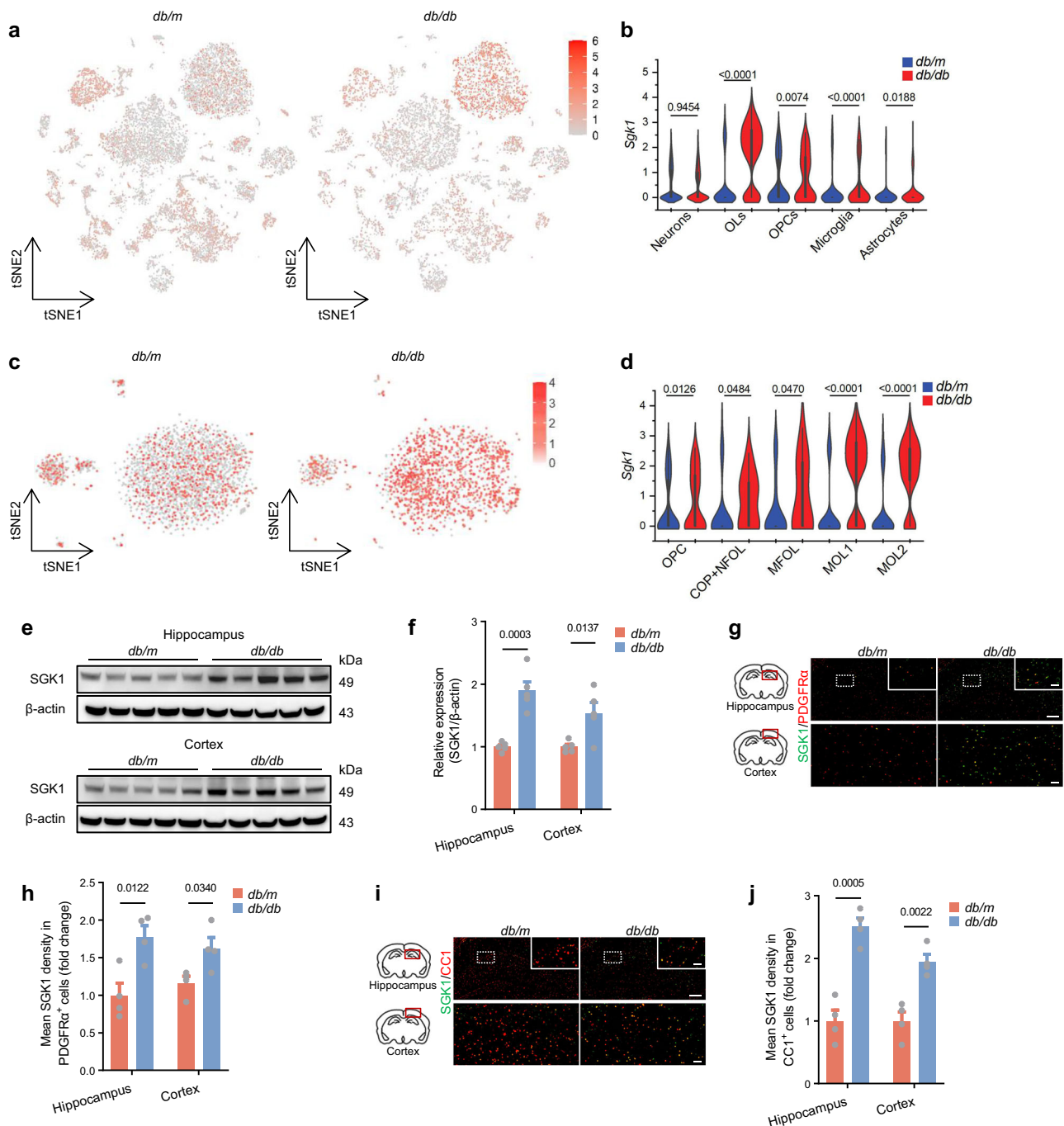


Fig. 6 | SGK1 expression was upregulated in the hippocampus in *db/db* mice. **a** t-SNE plot and **(b)** violin plot presenting the expression of *Sgk1* in the different cell types from the *db/m* and *db/db* mice. **c** t-SNE plot and **(d)** violin plot presenting the expression of *Sgk1* in the oligodendrocyte subclusters from the *db/m* and *db/db* mice. **e** Western blot analysis of the expression of SGK1 in control and diabetic mice. **f** Quantification of protein bands from **(e)**, $n = 5$ mice per group. **g** Representative immunofluorescence images of SGK1 and PDGFR α expression in

db/m and *db/db* mice. Scale bar: 200 μ m and 50 μ m (hippocampus), 50 μ m (cortex). **h** Quantification of immunofluorescence images from **(g)**, $n = 4$ mice per group. **i** Representative immunofluorescence images of SGK1 and CC1 expression in *db/m* and *db/db* mice. Scale bar: 200 μ m and 50 μ m (hippocampus), 50 μ m (cortex). **j** Quantification of immunofluorescence images from **(i)**, $n = 4$ mice per group. Data are presented as mean \pm SEM, and analyzed by unpaired two-tailed Student's *t*-tests. Source data are provided as a Source data file.

maintenance of myelin myelination. We also performed western blot analysis and immunofluorescence analysis to assess the protein level of SGK1. Consistent with the snRNA-seq analysis results, we verified that SGK1 was observably increased in both the hippocampus and cortex of *db/db* mice compared to those of *db/m* mice (Fig. 6e, f). Costaining for SGK1 and PDGFR α , we found the SGK1 fluorescence intensity within PDGFR α ⁺ cells increased in the hippocampus and

cortex of *db/db* mice compared to the *db/m* mice (Fig. 6g–h). As expected, the SGK1 intensity within CC1⁺ cells also increased in the *db/db* mice (Fig. 6i, j). The expression of SGK1 in OPCs and OLs was noticeably higher in HFD-fed mice than in the chow-fed group assessed by western blot and immunofluorescence experiments (Supplementary Fig. 14a–f). The expression of SGK1 in neurons did not been detected a significant up-regulation in *db/db* mice and HFD-fed mice

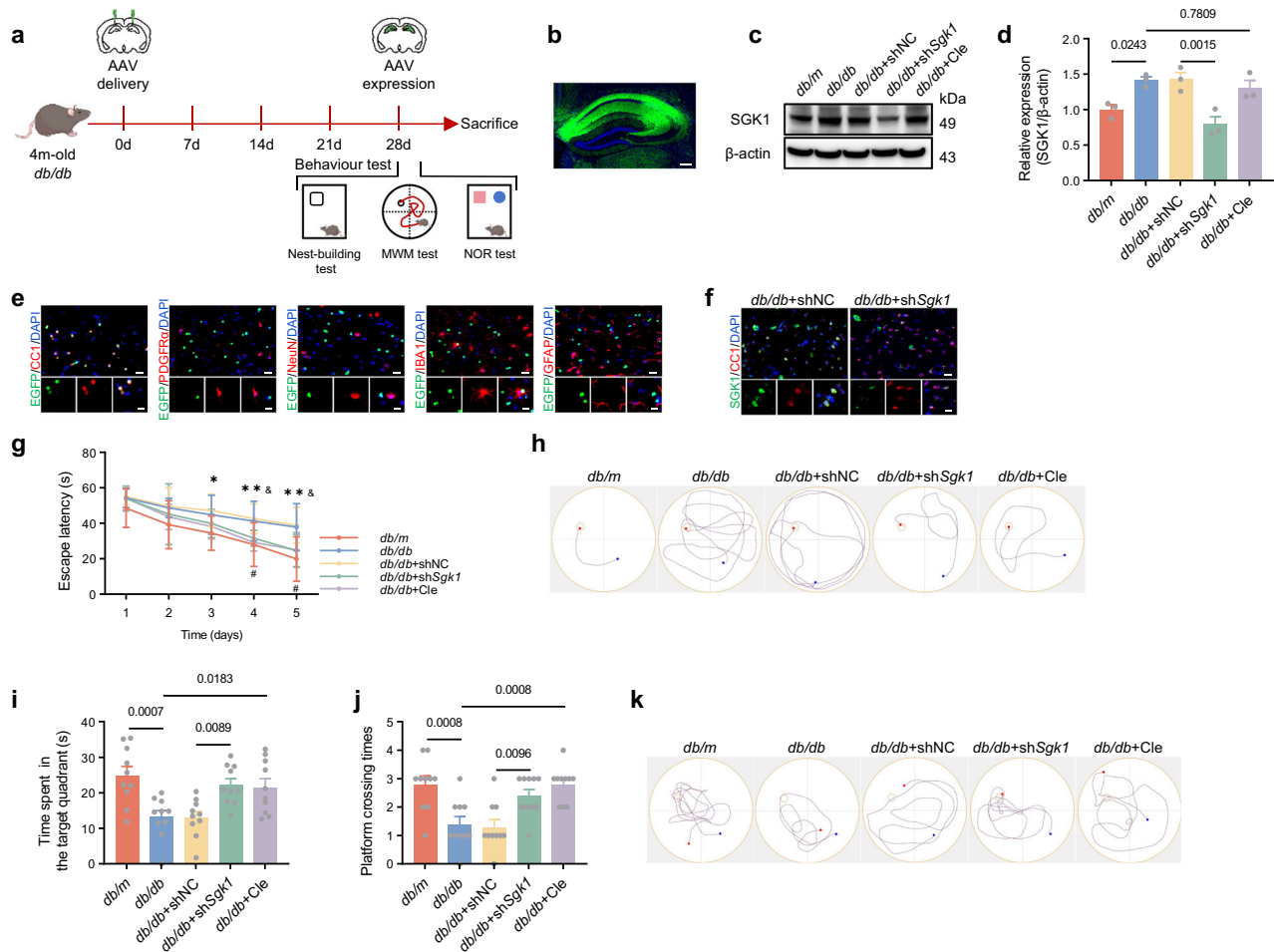


Fig. 7 | Specific SGK1 knockdown in OLs alleviated DACD in *db/db* mice.

a Schematic depicting the design of the AAV vector and the experimental timeline. **b** Fluorescence image of the section that expressed AAV in the hippocampus. Scale bar, 200μm. **c** Western blot analysis of the expression of SGK1 in different groups. **d** Quantification of protein bands from (c), $n = 3$ mice per group. **e** Representative immunofluorescence images of EGFP and cell markers (CCI, PDGFRα, NeuN, IBA1, GFAP) in *db/db*+shSGK1 groups. Scale bar: 20μm and 10μm. **f** Representative immunofluorescence images of SGK1 and CCI in *db/db*+shNC and *db/db*+shSGK1 groups. Scale bar: 20μm and 10μm. MWM test parameters, (g) escape latency, (h)

representative track plots in the learning phase, (i) time spent in the target quadrant, (j) times of mice passed through the platform location, (k) representative track plots in probe phase, $n = 10$ mice per group. Data are presented as mean \pm SEM, and analyzed by one way ANOVA followed by the Bonferroni post hoc test. * $p < 0.05$, ** $p < 0.01$, between *db/m* vs. *db/db*; # $p < 0.05$, between *db/db*+shNC vs. *db/db*+shSGK1; § $p < 0.05$, between *db/db* vs. *db/db*+Cle, in (g). Source data are provided as a Source data file. AAV, adeno-associated virus; Cle, clemastine; DACD, Diabetes-associated cognitive dysfunction; MWM test, Morris water-maze test; NOR test, novel object recognition test; OLs, oligodendrocytes.

(Supplementary Fig. 14g–j). Based on the results, we decided to focus on SGK1 for the following exploratory experiments. We hypothesized that up-regulated SGK1 expression in OLs might serve as a target to attenuate cognitive dysfunction in diabetes.

Specific SGK1 knockdown in OLs alleviates DACD in *db/db* mice

To clarify the effects of SGK1 in OLs on the anti-demyelination of DACD, we administered intrahippocampal recombinant adeno-associated virus (AAV) injection, which specifically inhibited SGK1 expression in OLs of *db/db* mice (Fig. 7a, b). Meanwhile, we implemented remyelination treatment (clemastine, 10 mg/kg, 14 d) for *db/db* mice to verify demyelination was the pivotal etiology of DACD. Western blot analysis results showed that SGK1 expression of the hippocampus was markedly decreased in the *db/db*+shSGK1 group compared to the *db/db*+shNC group, whereas clemastine treatment did not regulate the SGK1 expression in the *db/db*+Cle group (Fig. 7c, d). We detected the cell types expressing EGFP by staining with cell-specific markers for OLs (CCI), OPCs (PDGFRα), neurons (NeuN), microglia (IBA1), and astrocytes (GFAP). As shown in Fig. 7e, EGFP⁺ cells were mainly colocalized with CCI-labeled OLs rather than OPCs, neurons, microglia, or astrocytes. The expression rate of EGFP in OLs

ranged from 59.77% to 72.93% in the hippocampus. With the high specificity and efficiency, we confirmed the AAV exhibited satisfactory efficacy in transduction of OLs (Supplementary Fig. 15a, b). Then, we evaluated whether AAV regulated expression levels of SGK1 in diverse cells. The SGK1 intensity in CCI⁺ cells was distinctly down-regulated in the *db/db*+shSGK1 group compared to the *db/db*+shNC group (Fig. 7f and Supplementary Fig. 15c). Besides, immunofluorescence results showed that little change in SGK1 expression of OPCs, neurons, microglia, and astrocytes between the two groups (Supplementary Figs. 15d–g).

After 4 weeks of AAV injection, metabolic parameters and a battery of behavior tests were performed, which confirmed the neuro-protective function of knocking down SGK1 and clemastine treatment in cognitive deficit. SGK1 knockdown and clemastine therapy did not influence the body weights and fasting blood glucose of *db/db* mice (Supplementary Figs. 16a, b). The nest building test results indicated that both SGK1 knockdown and clemastine therapy improved spontaneous behaviors and motor function in *db/db* mice (Supplementary Fig. 16c). Both SGK1 knockdown and clemastine therapy enhanced the nonspatial memory assessed by NOR test (Supplementary Fig. 16d). In the MWM test, mice in *db/db*+shSGK1 group were found more excellent

cognitive performance compared to the *db/db*+shNC group, including shorter escape latency in the study phase, more extended time in the target quadrant and more times for crossing the platform location in probe phase (Fig. 7g–k). The results also presented that the clemastine therapy notably improved the cognitive dysfunction in the *db/db*+Cle group as expected. There were no significant differences in swim speeds and walking speeds in the *db/db* mice (Supplementary Figs. 16e, f).

Specific SGK1 knockdown in OLs promotes myelination via inhibiting NDRG1 phosphorylation in *db/db* mice

We observed demyelination of the hippocampus during the pathogenesis of DACD. We next evaluated the impact of SGK1 or clemastine

therapy on myelination in diabetic mice. The MBP immunofluorescence showed the fluorescence intensity of MBP in the hippocampus was increased in the *db/db*+shSgk1 group compared to the *db/db*+shNC group. On the other hand, clemastine therapy also improved the MBP expression in the hippocampus, compared to the *db/db* group (Fig. 8a, b). We received consistent results of MBP protein expression levels with western blotting (Fig. 8c, d). Similar results were found in the western blotting analysis of PSD95 expression (Fig. 8e, f).

We also performed the TEM to assess the ultra-structural myelination status of *db/db* mice. Similarly with the HFD-fed mice, the myelin sheath was thin and aberrant and the g-ratio was higher in the *db/db* group in comparison to those in *db/m* mice (Fig. 8g–i). Myelin damage in the hippocampus was extensively restored in *db/db*+shSgk1

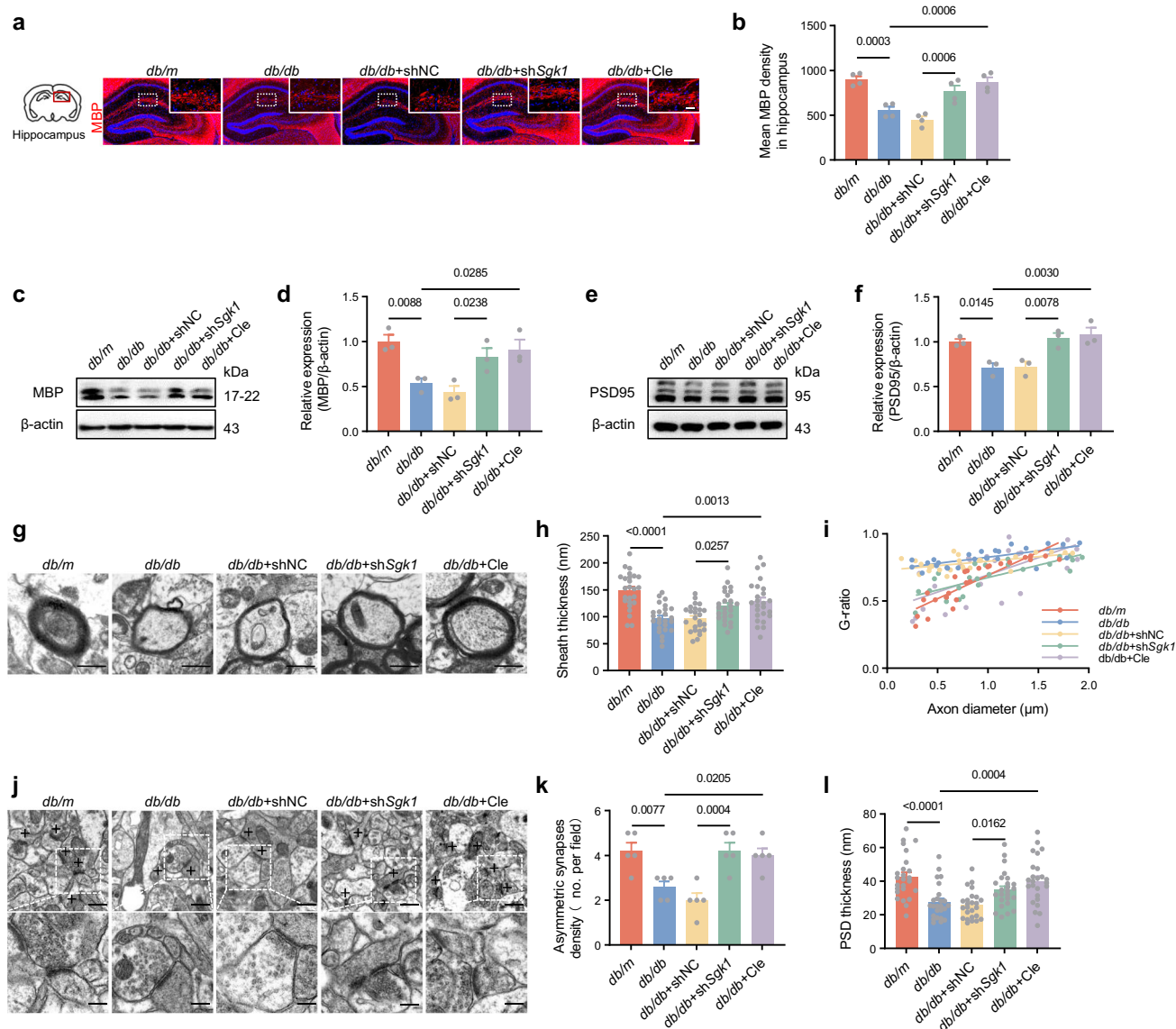


Fig. 8 | Specific SGK1 knockdown in OLs reversed demyelination in *db/db* mice.

a Representative immunofluorescence images of MBP expression in different groups. Scale bar: 200μm and 50μm. **b** Quantification of immunofluorescence images from (a), $n = 4$ mice per group. **c** Western blot analysis of the expression of MBP in different groups. **d** Quantification of protein bands from (c), $n = 3$ mice per group. **e** Western blot analysis of the expression of PSD95 in different groups. **f** Quantification of protein bands from (e), $n = 3$ mice per group. **g** Representative electron micrographs of myelinated axons of the hippocampus from different groups. Scale bar: 500 nm. **h** Bar chart showed sheath thickness from different

groups. **i** Scatter plot showed g-ratio from different groups. $n = 5$ images from 5 mice per group. **j** Representative electron micrographs of synapses of the hippocampus from different groups. Scale bar: 500 nm and 200 nm. **k** Bar chart showed the numbers of asymmetric synapses from different groups, $n = 5$ mice per group. **l** Bar chart showed PSD thickness from different groups, $n = 5$ images from 5 mice per group. Data are presented as mean \pm SEM, and analyzed by one way ANOVA followed by the Bonferroni post hoc test. Source data are provided as a Source data file. Cle, clemastine; OLs, oligodendrocytes.

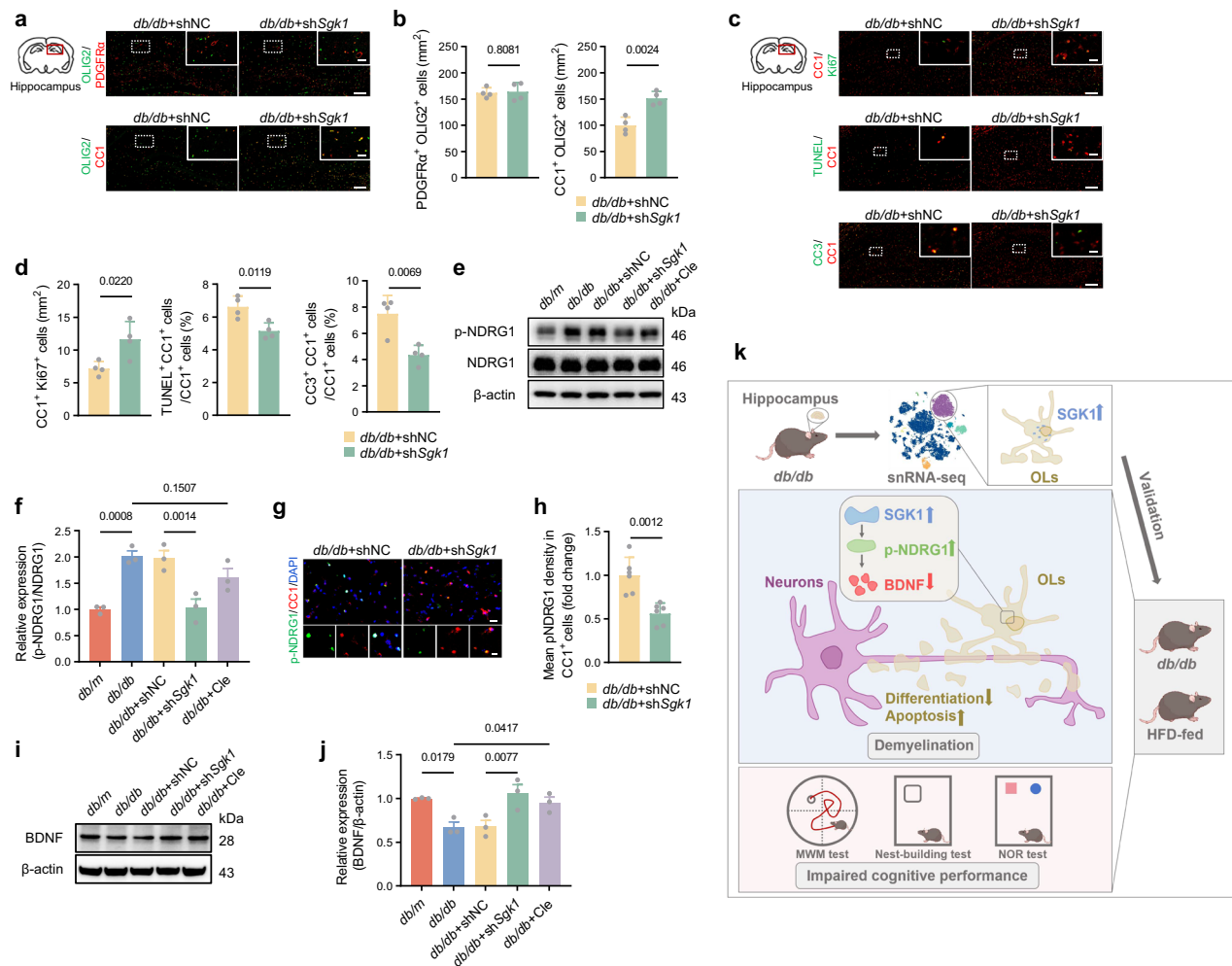


Fig. 9 | Specific SGK1 knockdown in OLS inhibited NDRG1 phosphorylation to promote myelination in *db/db* mice. **a** Representative immunofluorescence images of PDGFRα/OLIG2-labeling OPCs and CC1/OLIG2-labeling OLS in *db/db*+shNC and *db/db*+shSgk1 groups. Scale bar: 200μm and 50μm. **b** Quantification of immunofluorescence images from (a), *n* = 4 mice per group. **c** Representative immunofluorescence images of CC1/Ki67-labeling new OLS, CC1/TUNEL-labeling apoptotic OLS, and CC1/CC3-labeling apoptotic OLS in *db/db*+shNC and *db/db*+shSgk1 groups. Scale bar: 200μm and 25μm. **d** Quantification of immunofluorescence images from (c), *n* = 4 mice per group. **e** Western blot analysis of the expression of p-NDRG1 and NDRG1 in different groups. **f** Quantification of protein bands from (e), *n* = 3 mice per group. **g** Representative immunofluorescence

images of p-NDRG1 in CC1-labeling OLS in *db/db*+shNC and *db/db*+shSgk1 groups. Scale bar: 20μm and 10μm. **h** Quantification of protein bands from (g), *n* = 6 mice per group. **i** Western blot analysis of the expression of BDNF in different groups. **j** Quantification of protein bands from (i), *n* = 3 mice per group. **k** Schematic illustration elucidated the molecular mechanism underlying SGK1-related anti-demyelination efficacy in DACD. Data are presented as mean ± SEM, and analyzed by one way ANOVA followed by the Bonferroni post hoc test. Source data are provided as a Source data file. Cle, clemastine; DACD, diabetes-associated cognitive dysfunction; HFD, high-fat diet; MWM test, Morris water-maze test; NOR test, novel object recognition test; OLS, oligodendrocytes.

group and *db/db*+Cle group, compared with *db/db*+shNC group and *db/db* group, respectively, as implied by lower g-ratio (Fig. 8g–i). Moreover, the *db/db* mice were found synaptic deficits, including fewer asymmetric synapses per field and thinner postsynaptic density, compared to the *db/m* mice (Fig. 8j–l). The specific SGK1 knockdown in OLS and clemastine treatment could reverse the synaptic damage as expected (Fig. 8j–l). These findings showed SGK1 knockdown and clemastine therapy could reverse the demyelination and synaptic deficits induced by diabetes.

The reverse of hypermyelination phenotype in the SGK1 knockdown *db/db* mice might relate to transformations in the OLS pool. Therefore, immunofluorescence was implemented to quantify populations of OPCs and OLS. The numbers of OPCs did not change between the *db/db*+shNC group and *db/db*+shSgk1 group, while the quantity of CC1-labelled OLS was markedly increased in *db/db*+shSgk1 group (Fig. 9a, b). The number of new OLS (Ki67⁺CC1⁺ cells) was increased in the hippocampus after the SGK1 knockdown. Meanwhile,

SGK1 knockdown restrained the apoptotic OLS (TUNEL⁺CC1⁺ cells) induced by diabetes and diminished the cleaved caspase-3 (CC3, an apoptosis executioner) expression in OLS (Fig. 9c, d). These results collectively indicated that SGK1 played an important role in regulating OL differentiation and maintenance.

We further investigated the molecular mechanism underlying SGK1-related anti-demyelination efficacy in DACD. Studies have shown that NDRG1 is enriched in OLS and participates in myelination, plasticity, and axonal support. Considering that NDRG1 was one of the SGK1-specific targets and phosphorylation of NDRG1 was regulated by SGK1²⁷, we also assessed NDRG1 and phospho-NDRG1 expression in different groups. P-NDRG1 was significantly elevated in the *db/db* group compared to the *db/m* group, and p-NDRG1 was reduced in the *db/db*+shSgk1 group compared to the *db/db*+shNC group (Fig. 9e, f). According to the immunofluorescent staining results, the down-regulation of p-NDRG1 occurred in CC1-labeled OLS but not in OPCs, neurons, microglia, and astrocytes of *db/db*+shSgk1 group (Fig. 9g, h

and Supplementary Fig. 17). There was no difference of p-NDRG1 between *db/db* group and *db/db*+Cle group. BDNF, one of the most common neurotrophins, contributed to remyelination, plasticity synapses, neuronal development, and differentiation²⁸. A growing body of evidence suggested that BDNF acts as an intermediary between gene or drug therapy and improved neuroplasticity. Hence, we measured the BDNF expression of hippocampus in the 5 groups using the western blotting analysis. Compared to the control group, BDNF level was significantly decreased in the *db/db* group, whereas BDNF level was significantly increased in the *db/db*+sh*Sgk1* group and *db/db*+Cle group (Fig. 9i, j). We also verified that the SGK1/NDRG1/BDNF pathway was activated in the HFD-fed mice, another DACD mouse model (Supplementary Fig. 18). In summary, based on snRNA-seq and validation, this study demonstrated increased SGK1 of OLs inhibited BDNF expression via SGK1/NDRG1 pathway and aggravated demyelination in the hippocampus, eventually leading to DACD in diabetic mice (Fig. 9k).

Discussion

In this study, we used snRNA-seq technology to systematically delineate a high-resolution transcriptional landscape of hippocampus tissue at male diabetic mice status. DEGs analysis between the control and diabetic groups demonstrated gene transcription in each cell cluster underwent widespread diabetes-induced variation. Due to the unique shift of OLs, we further distinguished oligodendroglial lineage cell subtypes and characterized unique expression patterns of each OL subtype. We observed the abnormal dynamic changes of oligodendroglial lineage cells and myelin deposition in the hippocampus of male *db/db* and HFD-fed mice. Moreover, we found that SGK1, a key molecule involved in demyelination, was significantly highly expressed in OLs of the hippocampus in male diabetic mice. Combined with the experiments in vivo, we demonstrated increased SGK1 expression induced demyelination and DACD in a diabetic mouse model. Specific SGK1 knockdown in OLs rescued myelin impairment and DACD via inhibiting NDRG1 phosphorylation in male *db/db* mice. Therefore, these findings emphasized the relationship between demyelination and DACD progression. We also provided insights about the feasibility of targeting SGK1 and facilitating remyelination as a promising therapeutic approach of DACD.

The flourishing development of snRNA-seq transcription approaches has brought unprecedented resolution to examining of tissue samples; however, the application of this technique in hippocampus samples of diabetes animal models was still limited. Our team executed single-cell RNA sequencing (scRNA-seq) to explore the heterogeneity of hippocampal tissue in *db/db* mice and identified a subpopulation of pro-inflammatory disease-associated microglia in 2022²⁹. Xiang et al. also depicted transcriptional profile of hippocampal tissue in *db/db* mice using scRNA-seq in 2024³⁰, whereas the relevant report was brief and did not provide a detailed or comprehensive exhibition of scRNA-seq analysis data. Compared to scRNA-seq, the snRNA-seq technique bypassed the cell dissociation step and released the cell nucleus from intact cells using special detergents to capture and profile brain tissue cells comprehensively. For tissues that cannot easily dissociate into single-cell suspensions, such as brain tissue, snRNA-seq may be a better choice as it can minimize possible gene expression changes caused by dissociation. In addition, snRNA-seq analysis has higher sensitivity and generates more cell type classifications^{16,31}. Hence, we performed the snRNA-seq to characterize the composition and transcriptional changes in the hippocampus tissue of the diabetic mice model in order to fill the gap in this aspect.

Consistent with the previous research about the hippocampus using snRNA-seq, 7 cell types were identified in the present study^{32,33}. We conducted the DEGs analysis between the control group and the

diabetic group on the basis of different cell types. There were significant differences in the transcriptional characteristics of various cells, with neurons and astrocytes being the most prominent. KEGG analysis suggested that except for the commonly enriched pathways, the degree of enrichment in different pathways varied among different cell types. Our findings revealed specific cell types of corresponding KEGG pathways and provided more evidence for the function of individual cell types. It was worth noting that substantial experiments in vitro and in vivo were needed to verify further the diversity of the enrichment pathways in the future. Intriguingly, we noticed fewer cells in the hippocampus of the *db/db* mice than of the control group, which could be associated with diabetes-induced brain atrophy^{19,20}.

Myelin sheath that enfolds larger axons was formed by OLs in the CNS and Schwann cells in the peripheral nervous system³⁴. An OL formed a myelin sheath at the internodes of several adjacent axons to maintain information exchange and support the cellular function of the nervous system³⁵. Previous studies have shown that myelin degradation occurs in aging and neurodegenerative disorders (such as AD, PD, and amyotrophic lateral sclerosis). For example, myelin dysfunction accelerated A β plaque formation, which interfered with its maintenance and support effects on nervous system cells in the AD model^{14,36,37}. CNS myelin sulfatide deficiency induced disease-associated microglia and astrocytes, AD risk genes expression, and AD-like cognitive deficit in a mouse model of adult-onset myelin sulfatide deficiency³⁸. In summary, demyelinating injuries and myelin dysfunction were known to contribute to hallmark pathologies of AD and cognitive dysfunction.

Previous studies reported myelin damage induced by hyperglycemia and dyslipidemia played a critical role in the pathogenic mechanisms of diabetic peripheral neuropathy (such as sciatic nerve³⁹, sural nerve⁴⁰) and diabetic optic neuropathy⁴¹. A few studies measured myelin damage in the CNS at diabetic status. The latest neuroimaging study found that insulin resistance and insulin level were associated with altered myelin content, assessed by myelin water fraction in cognitively unimpaired adults¹². Another study showed myelin is critically damaged in the cerebral cortex of the streptozotocin-induced diabetic rat model through the detailed lipidomic analysis of myelin¹³. Given the interaction between peripheral nerve demyelination and diabetes, it was reasonable to surmise that demyelination also occurred in the central nervous system and finally resulted in neurodegeneration and cognitive impairment under hyperglycemic conditions.

In the current study, we focalized the dynamic change of OLs at the transcriptional level, highlighting the myelin-associated etiology of DACD by analyzing OLs subclusters. Consistent with the previous reports about the oligodendroglial lineage cells of brain tissue using snRNA-seq, we identified 5 distinct populations throughout OPC differentiation and OL maturation in the current study^{22,23,36}. Due to the brain tissue being collected from adult mice at the age of 20 weeks old in our study, populations of OPCs, COPs, NFOLs and MFOLs were considerably lower compared with those in juvenile mice, while mature OLs (MOL1 and MOL2) were higher. Diabetes distinctly altered OLs heterogeneity in the hippocampus. Our results elucidated molecular and cellular changes of OL subtypes in DACD via single-nucleus expression profiling analysis. We also identified abnormal expression genes in OL subtypes of DACD and characterized individual gene functions. Most of the myelination of the human brain is accomplished by the end of the second year of life, after which myelin is gradually lost with aging^{42,43}. In the adult brain, myelin generation still occurs to a lesser extent, OPCs maintain a dynamic balance in quantities and effectively respond to myelin loss by regulating proliferation and differentiation^{24,44}. After myelination, mature OLs require more energy to maintain the lipid-rich myelin membrane. However, a changing metabolic microenvironment, such as elevated lipid and iron levels, may make mature OLs vulnerable to

damage and even apoptosis^{45,46}. Mature OLs death and accompanying myelin loss lead to neuronal damage and functional deficits by suppressing the axonal neuroprotective function. We observed impaired OPC differentiation and aggravating OL apoptosis as characteristic pathological changes in diabetes mouse brains. Our results indicated that dysfunction of OLs and insufficient myelin regeneration were closely related to the onset and progression of DACD.

Based on the DEGs analysis between the *db/m* and *db/db* groups, *Sgk1* caught our attention due to its unique expression pattern and clustering characteristics. As the top DEG in hippocampal OLs of *db/db* mice, *Sgk1* was present predominantly in OLs and significantly up-regulated in hippocampal OLs of *db/db* mice. Previous studies confirmed that SGK1 was expressed at elevated levels in diabetes⁴⁷ and neurodegenerative diseases such as AD⁴⁸ and PD⁴⁹, and was associated with myelin formation⁵⁰. Therefore, we verified the unique expression feature of SGK1 in the hippocampus of diabetic mice and demonstrated the increased SGK1 aggravated the demyelination and cognitive impairment in the mice.

SGK1, a member of the AGC protein kinase family, had deleterious effects induced by glucocorticoids and aldosterone in the circulation. SGK1 expression was stimulated by glucocorticoids and mineralocorticoids, insulin, insulin-like growth factor 1, interleukin 6, transforming growth factor- β , follicle-stimulating hormone, and hepatic growth factor⁵¹. SGK1 was well acknowledged to play a pivotal role in maintaining cellular physiological activities, and the elevated SGK1 expression was associated with a variety of diseases, such as diabetes⁴⁷, hypertension⁵², neurodegenerative diseases⁴⁸ and cancers⁵³. SGK1 modified tau pathology via formation of SGK1-GSK-3 β -tau complex, resulting in neurodegeneration and poor cognitive performance in HFD-treated tauopathy model mice⁵⁴. Increased SGK1 induced pro-inflammatory properties of astrocytes and microglia, dopamine neuron degeneration via the multiple inflammatory pathways (NF- κ B and NLRP3 inflammasome) in PD animal models⁴⁹. SGK1 was overexpressed in the adipose tissue, intestine, vascular smooth muscle and myocardial tissue of diabetes models. Abnormally increased SGK1 inhibited insulin secretion via upregulating voltage-sensitive Kv1.5 channel and activating Na⁺/K⁺ ATPase during plasma membrane repolarization^{55,56}. SGK1 aggravated fluid retention and hypertension, induced deposition of matrix proteins resulting in diabetic complications. For example, SGK1 expression stimulated by hyperglycemia promoted renal Na⁺ transporters (such as epithelial sodium channel, sodium chloride cotransporter and Na⁺/K⁺-ATPase), which led to secondary hypertension and renal fibrosis⁵⁷. Increased SGK1 facilitated Na⁺ entry via the Na⁺/H⁺ exchanger 1 pathway, disrupting ion homeostasis and resulting in myocardial fibrosis and cardiac insufficiency^{58,59}. Consistent with previous clinical and experimental research, our findings showed SGK1 was a critical modulator of diabetes and diabetic complications.

The current study was meaningful in demonstrating myelin damage of the hippocampus and elucidated the mechanism underlying SGK1 and demyelination in DACD using a diabetic mice model. The majority of *Sgk1* was co-localized with *Mbp* at mRNA level in the corpus callosum of adult male rats exposed to acute stress⁶⁰. Another study reported SGK1 regulated pro-myelination indicators (BDNF, MBP, and Krox20) and was involved in remyelination in Schwann cells during peripheral nerve injury⁵⁰. As a SGK1-specific target, NDRG1 was enriched in myelinating OLs, modulated myelin damage and maintain myelin homeostasis^{61,62}. We found that abnormal SGK1 overexpression regulated OL differentiation, maturation and apoptosis, and then exacerbated demyelination via the NDRG1-mediated pathway, which provided powerful evidence of the modulation of SGK1 on myelination. We highlighted remyelination, and SGK1 may be potential therapeutic targets in nerve regeneration and DACD.

However, there were some limitations in our current study. First, the current study only described the transcriptional features in the mice at 20 weeks of age. Hippocampal snRNA-seq of *db/db* mice at different time points were needed to supplement to completely understanding of pseudotime trajectory toward the OLs in DACD progression. Second, our results were drawn from observations of male diabetic mice, possibly leading to gender bias in our conclusion. Moreover, considering the differences between animal and human hippocampus, further research was necessary to verify this information in other animal models and patients with DACD.

In summary, the current study provided a more in-depth insight into the transcriptional signatures and diversity of neuronal, glial cell populations in *db/db* mice of DACD progression. We emphasized that oligodendrogenesis and myelination played pivotal roles in DACD. In addition, our findings indicated that regulating the SGK1/NDRG1 pathway in OLs could reverse demyelination and DACD. Our work illuminated the molecular pathomechanism between demyelination and DACD and identified SGK1 as a potential therapeutic target for future antidementia medication development.

Methods

Animals

All mouse experiments were performed according to the Guidelines for the Care and Use of Laboratory Animals from the National Institutes of Health and were approved by the Animal Experimentation Ethics Committee of Shandong Provincial Hospital Affiliated to Shandong First Medical University (approval number: 2021-120). BKS.Cg-Dock7^m +/+Lepr^{db}/J mice were purchased from Changzhou Cavens Laboratory Animal Co., Ltd (Jiangsu, China). Wild-type C57BL/6J mice were purchased from Beijing HFK Bioscience Co., Ltd. The NG2-CreERT; Tau-mGFP and PLP-CreERT; mT/mG mice lines were gifted from Professor Feng Mei of the Third Military Medical University.

8-week-old male heterozygous *Lepr^{db/m}* (*db/m*) mice were identified as controls and homozygous *Lepr^{db/db}* (*db/db*) mice were diabetic. 8-week-old male wild-type C57BL/6J mice, NG2-CreERT; Tau-mGFP and PLP-CreERT; mT/mG mice were fed with a standard diet (10% Fat; Research Diets, D12450B) or a HFD (60% Fat; Research Diets, D12492) for 12 weeks to establish the DACD mouse model. Body weight and fasting blood glucose were recorded. After undergoing behavioural experiments, all mice were sacrificed for subsequent biochemical tests at 20 weeks of age. All mice were housed in a standard facility with an SPF environment under the 12 h light/12 h dark cycle at a room temperature of 22 °C \pm 2 °C, humidity of 55% \pm 5%, with ad libitum access to irradiated food and sterilized water.

Behavioral testing

Nest building test. Nest building test was performed to detect the spontaneous mouse behaviors⁶³. Each mouse was individually housed overnight (12 h) in a new standard cage with 6 pieces of nest material (5 cm \times 5 cm). The nest was evaluated according to the scoring standard: 4, ball-shaped or cup-shaped nest with a cover; 3, cup-shaped or bowl-shaped nest with sides; 2, platform-shaped nest in the cage; 1, no visible nest.

NOR test. The NOR test apparatus consisted of a square open field (45 cm \times 45 cm \times 45 cm). After the adaptation, each mouse was placed in the apparatus with two plastic object of the same color, size and shape on the bottom for 5 min. After 2 h, one of the objects was replaced by a novel object with different color, size, and shape and then, the mouse was placed in the apparatus for 5 min again. The discrimination index was calculated as a ratio of the time spent exploring the novel object to the total time spent exploring the novel and familiar objects using Video Tracker software (Anymaze, Varese, Italy)¹⁷.

MWM test. MWM test was known as a popular method to detect spatial learning and memory of mice³. The MWM system consisted of a circular tank (1.2 m diameter, 0.5 m height) filled with opaque white-colored water ($22.0 \pm 1.0^\circ\text{C}$) and a submerged platform (10 cm diameter, 1 cm under the water surface). During the learning phase, each mouse was released into the pool from pseudo-randomly selected starting positions to find the submerged platform within 60 s. If the mouse failed to locate the submerged platform, it can be guided to the platform and stand in 10 s. Learning trials were performed four times daily, 1 h apart for 5 consecutive days. During the probe phase, the submerged platform was removed, and each mouse was released into the pool to swim for 60 s. All tests were executed at fixed times (12:00 pm to 06:00 pm). Testing parameters were recorded and calculated using Video Tracker software (Anymaze, Varese, Italy).

snRNA-seq and analysis

Nucleus isolation and snRNA-seq. Mice were deeply anesthetized with isoflurane, and hippocampus tissues were rapidly dissected for snRNA-seq. Each group consisted of a mixture of the hippocampus of 6 mice. Collected fresh tissues were quickly cut to pieces, snap-frozen by liquid nitrogen and stored at -80°C . Genedenovo Biotechnology Co., Ltd (Guangzhou, China) administered nucleus isolation, sequencing and bioinformatic analysis under the guidance of 10X Genomics. Briefly, the samples were homogenized with ice-cold homogenization buffer (0.25 M sucrose, $5 \times 10^{-3}\text{ M}$ CaCl_2 , $3 \times 10^{-3}\text{ M}$ MgAc_2 , $10 \times 10^{-3}\text{ M}$ Tris-HCl (pH 8.0), $0.1 \times 10^{-3}\text{ M}$ EDTA, 1X protease inhibitor, and $1\text{ U } \mu\text{L}^{-1}$ RiboLock RNase inhibitor), the homogenates were filtered through a $70 \times 10^{-6}\text{ m}$ cell strainer and the cell nuclei were collected from a graded iodixanol solution series²¹. The cell nuclei were resuspended in resuspension buffer (0.04% bovine serum albumin, $0.2\text{ U } \mu\text{L}^{-1}$ RiboLock RNase inhibitor, $500 \times 10^{-3}\text{ M}$ mannitol and $0.1 \times 10^{-1}\text{ M}$ phenylmethanesulfonyl fluoride in PBS). After the quality control (the cell debris and large clumps were removed after the cell nuclei were filtered through a $40 \times 10^{-6}\text{ m}$ cell strainer), the concentration was adjusted to $700\text{--}1200$ nuclei μL^{-1} after manually assessed using trypan blue counterstaining and a hemocytometer. After gel beads-in-emulsion generation, libraries were generated and sequenced using the Chromium Next GEM Single Cell 3' Reagent Kit V3.1 on the 10X Genomics GemCode Single-cell instrument according to the instruction from the manufacturer^{31,64}.

Quality control and snRNA-seq data preprocessing. Raw sequencing data were converted and preprocessed by 10X Genomics Cell Ranger software V3.1.0 with the default parameters and aligned to the pre-mRNA reference (Ensemble_release 100, *Mus musculus*). Droplets with low-quality barcodes and unique molecular identifiers (UMI) were excluded. We also filtered cells with abnormal parameters using the DoubletFinder V2.0.3, such as gene counts out of the normal range ($500\text{--}4000$ per cell), UMIs ≥ 8000 , or mitochondrial gene percent $\geq 10\%$. Each cell gene expression by total expression was normalized by the global-scaling normalization method to produce normalized counts. The expression matrix was scaled and integrated.

Cell clustering. Graph-based clustering of snRNA-seq data was performed using Seurat V3.1.1. Cells were clustered using the Louvain method to maximize modularity, and these data were finally visualized using t-distributed stochastic neighbor embedding (t-SNE), which is a powerful tool for dimensionality reduction that is well-suited to visualizing high-dimensional data. According to the cell-type marker genes, 27 clusters were corresponded to 7 cell types.

Cell-cell communication analysis. To explore the difference in cell-cell communication in hippocampus cells of *db/db* mice, expression abundance of ligand-receptor analysis, number of ligand-receptor

analysis, and number of significantly enriched ligand-receptor analysis were executed using cellphoneDB V2.0. We constructed a cell-cell communication network based on the number of significantly enriched ligand-receptor pairs⁶⁵.

DEGs analysis. DEGs were identified based on the following criteria: $|\log_2\text{fold change}| > 0.36$, gene expression in $>25\%$ of cells in the target cluster, and p value < 0.05 . Relevant heat maps and violin maps were drawn using R package V.4.2.2. The DEGs were also analyzed for the KEGG statistically enriched pathways.

Cell lineage and pseudotime inference. Accurate lineage inference is a uniquely robust and flexible tool in identifying dynamic temporal gene expression. We ordered the OLs subclusters in pseudotime utilizing Slingshot, a novel method for inferring cell lineages, and pseudotime was used from single-cell gene expression data⁶⁶.

TMF administration

To induce Cre recombination, TMF (Selleck, S1238) was dissolved in sterile corn oil (Beyotime, ST2308). Then, 7-week-old male NG2-CreERT; Tau-mGFP and PLP-CreERT; mT/mG mice received TMF solution at a 100 mg/kg/day dose for successive 4 days through oral gavage²⁶. After 3 days of adaptation, these mice were fed with HFD to induce diabetes.

Clemastine administration

To investigate the demyelination in the hippocampus of diabetes, mice were administrated clemastine, a drug identified as promising for remyelination⁶⁷. 18-week-old *db/db* mice were treated with 10 mg/kg clemastine through intraperitoneal injection for 14 consecutive days (Selleck, S1847). Based on previous studies, the dose of clemastine was confirmed to promote myelination effectively⁶⁸. The mice of the clemastine treatment group received behavioral tests and tissue collection at 20 weeks of age, which was consistent with other groups.

Stereotaxic virus injection

Recombinant adeno-associated virus (AAV) was constructed for specific knockdown of SGK1 in mice OLs (OBIO Technology, Shanghai, China). pAAV-MBP-EGFP-miR30shRNA(*Sgk1*)-WP or pAAV-MBP-EGFP-miR30shRNA(NC)-WP were constructed for follow-up experiments. To construct the AAV vectors, the following sequence targeting the *Sgk1* mouse gene was used: $5'\text{-CGGCTGAGATGTACGACAATA-3}'$.

16-week-old mice were deeply anesthetized with isoflurane and fixed on the stereotaxic head frame (RWD Life Science, Shenzhen, China). Virus ($2\text{ } \mu\text{L}$, 10^9 vg) were injected bilaterally into the hippocampal region (at $\pm 1.5\text{ mm}$ mediolateral, -2 mm anteroposterior, -2 mm dorsoventral from the bregma) using a laboratory microsyringe at a rate of $0.1\text{ } \mu\text{L/min}$. After injection, the microsyringe needle was left for 5 min and then carefully and slowly removed. Behavioral tests and tissue collection were conducted 4 weeks after the viral injection.

Flow cytometry

20-week-old *db/db* and HFD-fed mice were anesthetized and sacrificed, and hippocampus tissues were rapidly collected and kept on ice. According to the instructions of the High Activity Adult Mouse and Rat Brain Enzymatic Digestion Kit (RWD, DHABE-5003), hippocampus tissues were digested by the Single Cell Suspension Dissociator (RWD, DSC-410) to maximize cell viability. We then resuspended the single cells in the ice-cold HBSS for further flow cytometric staining.

Single cells were incubated with mouse FcR blocking reagent (STARTER, SOB0599) for 15 min at room temperature. After being treated with LIVE/DEAD™ Fixable Near IR (780) Viability Kit (ThermoFisher, L34992) for 1 h at room temperature, cells were stained with fluorochrome-conjugated antibodies directed at cell surface antigens for 1 h at room temperature in the dark. For intracellular staining, cells

were fixed and permeabilized for 30 min at 4 °C in the dark by using the eBioscience™ Fxp3/Transcription Factor Staining Buffer Set (ThermoFisher, 00-5523-00). Then cells were washed and blocked prior to being incubated with relevant antibodies for 1 h at room temperature in the dark. Cell solutions were centrifuged at 450 g for 5 min at 4 °C and finally resuspended in fresh FACS buffer. Stained cell suspensions were detected utilizing Cytex Aurora 5-laser Spectra Analyzer (Cytex Biosciences, Shanghai, China), and the data were analyzed by Flowjo V10.8.1 software.

Immunofluorescence

Anesthetized mice were transcardially perfused with 0.01 M PBS followed by 4% paraformaldehyde. The whole brain was rapidly dissected and soaked in paraformaldehyde for 24 h and dehydrated in 30% sucrose. Then the tissue was embedded in optimal cutting temperature compound (OCT, SAKURA, 4583) and cut into 20 µm coronal brain sections by the cryostat microtome (Thermo Fisher Scientific, CryoStar NX50). The sections were antigen retrieval and blocked with 5% bovine serum albumin (Servicebio, GC305010). Sections were incubated with primary antibodies overnight at 4 °C. The sections were then probed with corresponding second antibodies at room temperature for 2 h. The sections were counterstained with 4',6-diamidino-2-phenylindole (DAPI, Beyotime, P0131) for identification of cell nuclei. Finally, the sections were examined and photographed by a fluorescence microscope (Nikon, Eclipse C1) with constant acquisition parameters, in order to compare different samples in the same experiment. The relative density of MBP immunostaining was measured and quantified from a constant field of view (FOV) utilizing by ImageJ software⁶⁹. All antibodies used in the present study were listed in Supplemental Table 1.

LFB

The whole brain was rapidly dissected and soaked in paraformaldehyde for 24 h. Then the fixed tissue was embedded in paraffin and cut into 4 µm coronal brain sections by microtome (Leica, CM1860). The sections were stained with LFB solution (Servicebio, G1030) at 60 °C for 4 h. After washing with PBS, differentiation with lithium carbonate solution, rehydration with a graded ethanol series, sections were immersed in xylene for 10 min and mounted with neutral glue. Finally, the sections were examined and photographed by an optional microscope (Nikon, E100).

FISH

Mice were deeply anesthetized with isoflurane, and fresh whole brains were collected, fixated in paraformaldehyde, dehydrated in 30% sucrose solution and embedded in an OCT compound. Brain tissues were cut into 10 µm slices. According to the manufacturer's instructions, a multiplex RNAscope was performed to detect gene expressions^{22,60}. The fluorescent photographs were captured by an optional microscope (Nikon, Eclipse ci).

EdU labelling and detection

To assess differentiation, 18-week-old diabetic and control mice received intraperitoneal injections with EdU (50 mg/kg, Beyotime, ST067) for 5 consecutive days. Mice were deeply anesthetized with isoflurane and sacrificed at 20 weeks of age. According to the manufacturer's recommendations, brain slices with cellular EdU were visualized using a BeyoClick™ EdU Cell Proliferation Assay (Beyotime, C0075S). The fluorescent photographs were captured by an optional microscope (Nikon, Eclipse ci).

TUNEL assays

To assess the apoptosis, TUNEL assays were executed using the TUNEL BrightRed Apoptosis Detection Kit (Vazyme, A113) according to the

manufacturer's direction. In brief, mice were deeply anesthetized with isoflurane, and fresh whole brains were collected, frozen sections were permeabilized and blocked with 5% bovine serum albumin for 1 h at room temperature. After equilibration, brain slices were treated with TdT working solution for 1 h at 37 °C. Finally, the slices were incubated with relative primary antibodies for further immunofluorescence experiments.

TEM

Mice were deeply anesthetized with isoflurane, and fresh hippocampus tissue was immediately collected and soaked in a pre-cooling fixative solution (2.5% glutaraldehyde) at 4 °C for 18 h. Then the tissue was post-fixed in 1% osmium tetroxide at room temperature for 2 h in the dark. After rehydration with a graded ethanol and acetone series, they were embedded in an acetone-resin mixture. The resin blocks were sectioned ultrathin at 60 to 80 nm on an ultrathin microtome; ultrathin sections were collected on 150-slot copper grids and stained with 2% uranyl acetate and 2.6% lead citrate solution. Finally, the sections were examined and photographed under an electron microscope (Hitachi, HT7800). The myelinated fiber g-ratio is the ratio of the inner to the outer diameter of the axon myelin sheath.

Western blotting

Mice were anesthetized, and fresh hippocampus and cortex tissue was rapidly dissected for Western blotting. The brain tissue was homogenized in Protein Extraction Reagent (Beyotime, P0033) to exact protein. The protein concentrations were measured by bicinchoninic acid assay (Beyotime, P0009). 50 µg of total protein was resolved by 10%-15% sodium dodecyl sulfate-polyacrylamide gel electrophoresis and transferred to sodium dodecyl sulfate-polyacrylamide gel electrophoresis membranes. The membranes were incubated with appropriate antibodies, and the immunoreactive bands were detected and visualized by the chemiluminescence system (Bio-Rad, chemidoc MP imaging system). All antibodies used in the present study were listed in Supplemental Table 1.

Statistical analysis

Sample size was chosen based on experience with the used experimental models. No statistical method was used to determine animal's sample size. All results were presented as mean ± SEM. A normality test was carried out whenever possible to choose appropriate statistical analysis. Data were analyzed by GraphPad Prism V8.0 software. A two-tailed *p* value less than 0.05 was considered statistically significant. The details for each experiment, the number of replicates and statistical specifications are indicated in the figure legends, results, and the Source Data file.

Reporting summary

Further information on research design is available in the Nature Portfolio Reporting Summary linked to this article.

Data availability

The mouse single-nucleus RNA sequencing data generated in this study have been deposited in the CNGB Sequence Archive (CNSA) of China National GeneBank DataBase (CNGBdb) under accession code [CNP0004961](https://cn.gdb.cn/CNP0004961). All other data generated in this study are provided in the Supplementary Information and Source Data file. Source data are provided with this paper.

Code availability

Codes used in this manuscript can be downloaded at https://github.com/apanhui/scRNA_analysis_mmu.

References

- Khunti, K. et al. Diabetes and multiple long-term conditions: a review of our current global health challenge. *Diab care* **46**, 2092–2101 (2023).
- Biessels, G. J. & Despa, F. Cognitive decline and dementia in diabetes mellitus: mechanisms and clinical implications. *Nat. rev. Endocrinol.* **14**, 591–604 (2018).
- Li, Q. et al. Impaired lipophagy induced-microglial lipid droplets accumulation contributes to the buildup of TREM1 in diabetes-associated cognitive impairment. *Autophagy* **19**, 2639–2656 (2023).
- Biessels, G. J. & Whitmer, R. A. Cognitive dysfunction in diabetes: how to implement emerging guidelines. *Diabetologia* **63**, 3–9 (2020).
- Kullmann, S. et al. Brain insulin resistance at the crossroads of metabolic and cognitive disorders in humans. *Physiol. Rev.* **96**, 1169–1209 (2016).
- Biessels, G. J., Nobili, F., Teunissen, C. E., Simó, R. & Scheltens, P. Understanding multifactorial brain changes in type 2 diabetes: a biomarker perspective. *Lancet Neurol.* **19**, 699–710 (2020).
- Launer, L. J. et al. Effects of intensive glucose lowering on brain structure and function in people with type 2 diabetes (ACCORD MIND): a randomised open-label substudy. *Lancet Neurol.* **10**, 969–977 (2011).
- van Sloten, T. T., Sedaghat, S., Carnethon, M. R., Launer, L. J. & Stehouwer, C. D. A. Cerebral microvascular complications of type 2 diabetes: stroke, cognitive dysfunction, and depression. *Lancet Diab Endocrinol.* **8**, 325–336 (2020).
- Koekkoek, P. S., Kappelle, L. J., van den Berg, E., Rutten, G. E. & Biessels, G. J. Cognitive function in patients with diabetes mellitus: guidance for daily care. *Lancet Neurol.* **14**, 329–340 (2015).
- Sima, A. A. & Zhang, W. Mechanisms of diabetic neuropathy: axon dysfunction. *Handb. Clin. Neurol.* **126**, 429–442 (2014).
- Palavicini, J. P. et al. Early disruption of nerve mitochondrial and myelin lipid homeostasis in obesity-induced diabetes. *JCI insight* **5**, e137286 (2020).
- O'Grady, J. P. et al. Elevated insulin and insulin resistance are associated with altered myelin in cognitively unimpaired middle-aged adults. *Obes. (Silver Spring)* **27**, 1464–1471 (2019).
- Cermenati, G. et al. Diabetes alters myelin lipid profile in rat cerebral cortex: protective effects of dihydropyrogesterone. *J. Steroid Biochem Mol. Biol.* **168**, 60–70 (2017).
- Depp, C. et al. Myelin dysfunction drives amyloid- β deposition in models of Alzheimer's disease. *Nature* **618**, 349–357 (2023).
- Sun, C. et al. Nonenzymatic function of DPP4 in diabetes-associated mitochondrial dysfunction and cognitive impairment. *Alzheimers Dement* **18**, 966–987 (2022).
- Ding, J. et al. Systematic comparison of single-cell and single-nucleus RNA-sequencing methods. *Nat. biotechnol.* **38**, 737–746 (2020).
- Little, K. et al. Disruption of cortical cell type composition and function underlies diabetes-associated cognitive decline. *Diabetologia* **66**, 1557–1575 (2023).
- Zhuang, H. et al. Long-term high-fat diet consumption by mice throughout adulthood induces neurobehavioral alterations and hippocampal neuronal remodeling accompanied by augmented microglial lipid accumulation. *Brain Behav. Immun.* **100**, 155–171 (2022).
- Yang, X. Y. et al. Berberine improves cognitive impairment by alleviating brain atrophy and promoting white matter reorganization in diabetic db/db mice: a magnetic resonance imaging-based study. *Meta Brain Dis.* **39**, 941–952 (2024).
- Infante-Garcia, C. et al. Mango leaf extract improves central pathology and cognitive impairment in a type 2 diabetes mouse model. *Brain Pathol.* **27**, 499–507 (2017).
- Yao, Y. et al. Pyruvate dehydrogenase kinase 1 protects against neuronal injury and memory loss in mouse models of diabetes. *Cell Death Dis.* **14**, 722 (2023).
- Marques, S. et al. Oligodendrocyte heterogeneity in the mouse juvenile and adult central nervous system. *Science* **352**, 1326–1329 (2016).
- Park, H. et al. Single-cell RNA-sequencing identifies disease-associated oligodendrocytes in male APP NL-G-F and 5XFAD mice. *Nat. Commun.* **14**, 802 (2023).
- Long, K. L. P., Breton, J. M., Barraza, M. K., Perloff, O. S. & Kaufer, D. Hormonal regulation of oligodendrogenesis I: effects across the lifespan. *Biomolecules* **11**, 283 (2021).
- Chen, J. F. et al. Enhancing myelin renewal reverses cognitive dysfunction in a murine model of Alzheimer's disease. *Neuron* **109**, 2292–2307 (2021).
- Cheng, Y. J. et al. Prolonged myelin deficits contribute to neuron loss and functional impairments after ischaemic stroke. *Brain* **147**, 1294–1311 (2024).
- Sahin, P., McCaig, C., Jeevahan, J., Murray, J. T. & Hainsworth, A. H. The cell survival kinase SGK1 and its targets FOXO3a and NDRG1 in aged human brain. *Neuropathol. Appl Neurobiol.* **39**, 623–633 (2013).
- Xiao, J. Thirty years of BDNF study in central myelination: From biology to therapy. *J. Neurochem* **167**, 321–336 (2023).
- Ma, S. et al. Single-Cell sequencing analysis of the db/db mouse hippocampus reveals cell-type-specific insights into the pathobiology of diabetes-associated cognitive dysfunction. *Front Endocrinol. (Lausanne)* **13**, 891039 (2022).
- Xiang, Q. et al. Heterogeneity and synaptic plasticity analysis of hippocampus based on db(-/-) mice induced diabetic encephalopathy. *Psychoneuroendocrinology* **159**, 106412 (2024).
- Wang, M. et al. Guidelines for bioinformatics of single-cell sequencing data analysis in Alzheimer's disease: review, recommendation, implementation and application. *Mol. Neurodegener.* **17**, 17 (2022).
- Habib, N. et al. Disease-associated astrocytes in Alzheimer's disease and aging. *Nat. Neurosci.* **23**, 701–706 (2020).
- Su, Y. et al. A single-cell transcriptome atlas of glial diversity in the human hippocampus across the postnatal lifespan. *cell stem cell* **29**, 1594–1610.e1598 (2022).
- Figlia, G., Gerber, D. & Suter, U. Myelination and mTOR. *Glia* **66**, 693–707 (2018).
- Simons, M. & Nave, K. A. Oligodendrocytes: myelination and axonal support. *Cold Spring Harb. Perspect. Biol.* **8**, a020479 (2015).
- Desai, M. K. et al. Triple-transgenic Alzheimer's disease mice exhibit region-specific abnormalities in brain myelination patterns prior to appearance of amyloid and tau pathology. *Glia* **57**, 54–65 (2009).
- Desai, M. K. et al. Early oligodendrocyte/myelin pathology in Alzheimer's disease mice constitutes a novel therapeutic target. *Am. J. Pathol.* **177**, 1422–1435 (2010).
- Qiu, S. et al. Adult-onset CNS myelin sulfatide deficiency is sufficient to cause Alzheimer's disease-like neuroinflammation and cognitive impairment. *Mol. neurodegeneration* **16**, 64 (2021).
- Fan, B. et al. Mesenchymal stromal cell-derived exosomes ameliorate peripheral neuropathy in a mouse model of diabetes. *Diabetologia* **63**, 431–443 (2020).
- Peltier, A., Goutman, S. A. & Callaghan, B. C. Painful diabetic neuropathy. *BMJ* **348**, g1799 (2014).
- Wu, H. et al. Deficient deposition of new myelin impairs adult optic nerve function in a murine model of diabetes. *Glia* **71**, 1333–1345 (2023).
- Zota, I., Chanoumidou, K., Charalampopoulos, I. & Gravanis, A. Dynamics of myelin deficits in the 5xFAD mouse model for Alzheimer's disease and the protective role of BDNF. *Glia* **72**, 809–827 (2024).

43. Buyanova, I. S. & Arsalidou, M. Cerebral white matter myelination and relations to age, gender, and cognition: a selective review. *Front Hum. Neurosci.* **15**, 662031 (2021).
44. Hughes, E. G., Kang, S. H., Fukaya, M. & Bergles, D. E. Oligodendrocyte progenitors balance growth with self-repulsion to achieve homeostasis in the adult brain. *Nat. Neurosci.* **16**, 668–676 (2013).
45. Butts, B. D., Houde, C. & Mehmet, H. Maturation-dependent sensitivity of oligodendrocyte lineage cells to apoptosis: implications for normal development and disease. *Cell Death Differ.* **15**, 1178–1186 (2008).
46. Zhang, T. et al. Autophagy collaborates with apoptosis pathways to control oligodendrocyte number. *Cell Rep.* **42**, 112943 (2023).
47. Yang, C. et al. The functional duality of SGK1 in the regulation of hyperglycemia. *Endocr. Connect* **9**, R187–R194 (2020).
48. Cao, Q. et al. Targeting histone K4 trimethylation for treatment of cognitive and synaptic deficits in mouse models of Alzheimer's disease. *Sci. Adv.* **6**, eabc8096 (2020).
49. Kwon, O. C. et al. SGK1 inhibition in glia ameliorates pathologies and symptoms in Parkinson disease animal models. *EMBO Mol. Med* **13**, e13076 (2021).
50. Okura, A. et al. SGK1 in Schwann cells is a potential molecular switch involved in axonal and glial regeneration during peripheral nerve injury. *Biochem Biophys. Res Commun.* **607**, 158–165 (2022).
51. Lang, F., Strutz-Seeböhm, N., Seeböhm, G. & Lang, U. E. Significance of SGK1 in the regulation of neuronal function. *J. Physiol.* **588**, 3349–3354 (2010).
52. Sierra-Ramos, C. et al. SGK1 activation exacerbates diet-induced obesity, metabolic syndrome and hypertension. *J. Endocrinol.* **244**, 149–162 (2020).
53. Zhu, R. et al. The prospect of serum and glucocorticoid-inducible kinase 1 (SGK1) in cancer therapy: a rising star. *Ther. Adv. Med Oncol.* **12**, 1758835920940946 (2020).
54. Elahi, M. et al. High-fat diet-induced activation of SGK1 promotes Alzheimer's disease-associated tau pathology. *Hum. Mol. Genet* **30**, 1693–1710 (2021).
55. Ullrich, S. et al. Serum- and glucocorticoid-inducible kinase 1 (SGK1) mediates glucocorticoid-induced inhibition of insulin secretion. *Diabetes* **54**, 1090–1099 (2005).
56. Ullrich, S. et al. Dexamethasone increases Na⁺/K⁺ ATPase activity in insulin secreting cells through SGK1. *Biochem Biophys. Res Commun.* **352**, 662–667 (2007).
57. Lang, F. & Shumilina, E. Regulation of ion channels by the serum- and glucocorticoid-inducible kinase SGK1. *FASEB J.* **27**, 3–12 (2013).
58. Lee, S. G. et al. Dapagliflozin attenuates diabetes-induced diastolic dysfunction and cardiac fibrosis by regulating SGK1 signaling. *BMC Med* **20**, 309 (2022).
59. Voelkl, J. et al. Sgk1 sensitivity of Na⁽⁺⁾/H⁽⁺⁾ exchanger activity and cardiac remodeling following pressure overload. *Basic Res Cardiol.* **107**, 236 (2012).
60. Hinds, L. R. et al. Dynamic glucocorticoid-dependent regulation of Sgk1 expression in oligodendrocytes of adult male rat brain by acute stress and time of day. *PLoS One* **12**, e0175075 (2017).
61. Marechal, D. et al. N-myc downstream regulated family member 1 (NDRG1) is enriched in myelinating oligodendrocytes and impacts myelin degradation in response to demyelination. *Glia* **70**, 321–336 (2022).
62. Heller, B. A. et al. Functionally distinct PI 3-kinase pathways regulate myelination in the peripheral nervous system. *J. Cell Biol.* **204**, 1219–1236 (2014).
63. Xiong, X. D., Xiong, W. D., Xiong, S. S. & Chen, G. H. Age- and gender-based differences in nest-building behavior and learning and memory performance measured using a radial six-armed water maze in C57BL/6 mice. *Behav. Neurol.* **2018**, 8728415 (2018).
64. Kim, N., Kang, H., Jo, A., Yoo, S. A. & Lee, H. O. Perspectives on single-nucleus RNA sequencing in different cell types and tissues. *J. Pathol. transl. Med* **57**, 52–59 (2023).
65. Niu, T. et al. Pathogenesis study based on high-throughput single-cell sequencing analysis reveals novel transcriptional landscape and heterogeneity of retinal cells in type 2 diabetic mice. *Diabetes* **70**, 1185–1197 (2021).
66. Street, K. et al. Slingshot: cell lineage and pseudotime inference for single-cell transcriptomics. *BMC Genomics* **19**, 477 (2018).
67. Zhu, J., Ma, R. & Li, G. Drug repurposing: clemastine fumarate and neurodegeneration. *Biomed. pharmacother.* **157**, 113904 (2023).
68. Li, Y. et al. The Eph receptor A4 plays a role in demyelination and depression-related behavior. *J. Clin. Invest* **132**, e152187 (2022).
69. Vanzulli, I. et al. Disruption of oligodendrocyte progenitor cells is an early sign of pathology in the triple transgenic mouse model of Alzheimer's disease. *Neurobiol. Aging* **94**, 130–139 (2020).

Acknowledgements

We acknowledge Professor Feng Mei of the Third Military Medical University (Army Medical University) for guiding this subject and providing us with the NG2-CreERT; Tau-mGFP and PLP-CreERT; mT/mG mice. We also acknowledge Professor Fuchou Tang of Peking University for providing guidance on the snRNA-seq part. We are grateful to Guangzhou Genedenovo Biotechnology Co., Ltd for assisting in sequencing and bioinformatics analysis. This work was supported by National Natural Science Foundation of China (82471206, 82000771 to Q.Q.Y., 82401487 to Z.Y.J., and 82288101 to L.L.), STI2030-Major Projects (2021ZD0200800 to L.L.), Postdoctoral Fellowship Program of CPSF (GZC20231741 to Z.Y.J.), China Postdoctoral Science Foundation (2024M762178 to Z.Y.J.), Shandong Provincial Youth Innovation Team Development Plan of Colleges and Universities (2022KJ193 to Q.Q.Y.), Beijing Postdoctoral Research Fund (to Z.Y.J.), Shandong Provincial Natural Science Foundation (ZR2021MH014 to S.B.L., ZR2021MH043 to B.L.), and Young Elite Sponsorship Program of Shandong Provincial Medical Association (2023_LC_0133 to Q.Q.Y.).

Author contributions

Z.Y.J., J.W.H., L.L. and Q.Q.Y. conceived and designed the study. Z.Y.J., B.L. and T.S.L. carried out the majority of experiments. R.J.L., S.B.L., S.X., X.Y.W., Y.F.W., Z.F.G. and P.Q.Z. contributed to data collection and provided experimental support. Z.Y.J., R.J.L., M.N.Z. and X.N.W. analyzed and interpreted the data. Z.Y.J. and Q.Q.Y. prepared the manuscript. Z.Y.J., B.L., T.S.L., X.X.L., K.Y., M.N.Z., X.N.W., Z.Y.Z., J.W.H., L.L. and Q.Q.Y. revised and edited the manuscript. All authors revised the manuscript and approved the final version.

Competing interests

The authors declare no competing interests.

Additional information

Supplementary information The online version contains supplementary material available at <https://doi.org/10.1038/s41467-025-56854-2>.

Correspondence and requests for materials should be addressed to Junwei Hao, Lin Lu or Qingqing Yin.

Peer review information *Nature Communications* thanks the anonymous reviewers for their contribution to the peer review of this work. A peer review file is available.

Reprints and permissions information is available at <http://www.nature.com/reprints>

Publisher's note Springer Nature remains neutral with regard to jurisdictional claims in published maps and institutional affiliations.

Open Access This article is licensed under a Creative Commons Attribution-NonCommercial-NoDerivatives 4.0 International License, which permits any non-commercial use, sharing, distribution and reproduction in any medium or format, as long as you give appropriate credit to the original author(s) and the source, provide a link to the Creative Commons licence, and indicate if you modified the licensed material. You do not have permission under this licence to share adapted material derived from this article or parts of it. The images or other third party material in this article are included in the article's Creative Commons licence, unless indicated otherwise in a credit line to the material. If material is not included in the article's Creative Commons licence and your intended use is not permitted by statutory regulation or exceeds the permitted use, you will need to obtain permission directly from the copyright holder. To view a copy of this licence, visit <http://creativecommons.org/licenses/by-nc-nd/4.0/>.

© The Author(s) 2025